Adding geometry to fingerprinting localization with Euclidean Distance Matrix (EDM)

Robin Solignac

Master Thesis
Systems of Communication
Submitted 15 march 2019
École Polytechnique Fédérale de Lausanne, IC faculty

LCAV
Swisscom Digital Lab

Supervisors:
Adam Scholefield, LCAV
Guillermo Barrenetxea, Swisscom

Lausanne, EPFL, 2019

Wings are a constraint that makes
it possible to fly.
— Robert Bringhurst

To my parents…

Abstract

Lorem ipsum dolor sit amet, consectetuer adipiscing elit. Ut purus elit, vestibulum ut, placerat ac, adipiscing vitae, felis. Curabitur dictum gravida mauris. Nam arcu libero, nonummy eget, consectetuer id, vulputate a, magna. Donec vehicula augue eu neque. Pellentesque habitant morbi tristique senectus et netus et malesuada fames ac turpis egestas. Mauris ut leo. Cras viverra metus rhoncus sem. Nulla et lectus vestibulum urna fringilla ultrices. Phasellus eu tellus sit amet tortor gravida placerat. Integer sapien est, iaculis in, pretium quis, viverra ac, nunc. Praesent eget sem vel leo ultrices bibendum. Aenean faucibus. Morbi dolor nulla, malesuada eu, pulvinar at, mollis ac, nulla. Curabitur auctor semper nulla. Donec varius orci eget risus. Duis nibh mi, congue eu, accumsan eleifend, sagittis quis, diam. Duis eget orci sit amet orci dignissim rutrum.

Nam dui ligula, fringilla a, euismod sodales, sollicitudin vel, wisi. Morbi auctor lorem non justo. Nam lacus libero, pretium at, lobortis vitae, ultricies et, tellus. Donec aliquet, tortor sed accumsan bibendum, erat ligula aliquet magna, vitae ornare odio metus a mi. Morbi ac orci et nisl hendrerit mollis. Suspendisse ut massa. Cras nec ante. Pellentesque a nulla. Cum sociis natoque penatibus et magnis dis parturient montes, nascetur ridiculus mus. Aliquam tincidunt urna. Nulla ullamcorper vestibulum turpis. Pellentesque cursus luctus mauris.

Key words:

Contents

List of Figures

List of Tables

1 Introduction

1.1 Introduction

The wide variety of rocks that forms the earth crust makes it challenging to model. Each formation that exist beneath us can in itself be considered as different materials, with diverse mineralogy, geological histories and behavior. However, their one common thread is a composite structure formed by minerals, pores and cracks [1]. Years of worldwide experimentations on these materials already showed similarities in results, through the definition of material parameters used to characterize their behavior. Analysis and interpretation of these experimental outcomes are key elements in the understanding of rock response, and enables safer prediction of their behavior, which is used in the design of geotechnical structures.

Rock response under a certain state of stress is associated with material strength and is often characterized by its failure. Multiple experiments, such as conventional triaxial and multiaxial tests, were developed with the aim of getting more information on the various states of stress that leads to rock failure. However, site-specific rock engineering properties are often not available during the preliminary design phase of structures constructed on or into the rock mass. Therefore, predictive models are widely used in initial stage of the design for prediction of the engineering properties of rock mass which may have an empirical or theoretical nature.

Over the last century, many predictive models have been developed. They describe planes in the σ_1-σ_2-σ_3 space that approximate experiments data using material parameters. The plethora of failure criterion theories respond to the challenge of finding one that can give the most accurate description of rock behavior. Empirical models are usually developed for a specific rock type or rock formation and therefore, need to be evaluated before they can be applied to estimate the properties of rock masses that were not included in the data used for their development. Theoretical models have been developed to rigorously estimate the stress state at which rocks experience failure [1]. Such models are often developed based on fundamental aspects of rock mechanics and there are applicable to a wider range of rocks and rock formations.

The most well-known and widely used failure criterion is the Mohr-Coulomb model, which provides a linear relationship between the normal stress and stress strength of materials. The failure envelop is characterized using the friction angle ϕ and the cohesion intercept c [4]. Other criterion, such as the Hoek-Brown model for intact rocks and rock masses, are empirical and non-linear [3]. They give relatively reasonable approximation of the state of stress at failure, especially for low values confining stress (i.e., minor principal stress, σ_3). These failure criteria may be written in terms of the major (σ_1) and minor (σ_3) principal stresses, without any consideration to effect of intermediate principal stress (σ_2).

1.2 Limitation of current failure criteria and motivation

Experiments, however, have shown that the intermediate principal stress affects the mode of failure and the major principal stresses that are developed when the rock mass fails [1, 5, 3, 6]. Moreover, the failure envelop that describe best the experiments data isn't linear and can hardly be well approximated with only one plane.

To address the limitations of the simple failure criteria such as that of Mohr-Coulomb, and following the pioneering work of Paul (1968), other investigators, developed a more comprehensive failure criterion that accounts for the three principal stresses, , and (resp. major, intermediate and minor stresses) [7, 8]. The bi-linear failure envelop defined by the criterion enables a more accurate prediction of the rock behavior, especially at high stress states.

This new approach to representation of the rock failure and the corresponding stress state, however, requires model material constants to be evaluated and calibrated using the laboratory tests such those introduced by Labuz et al. 1996 [5] and Zeng et al. 2019 [3]. Experimentation is a key element in the quest for the most accurate failure criterion, as it accounts for the real response of rocks. In order to be recognized as accurate, the criterion should provide a failure envelop that gives good prediction and approximation of the test results. It is also important that the chosen experiments are diverse and representative of the real state of stress and strain that the rock could undergo. Indeed, a failure criterion well suited for the prediction of a particular test, could lead to a wrong estimation for another test. Therefore, additional test data will help to provide a more accurate prediction of the and evaluation of the model parameters for the failure criterion proposed by Paul (1968) [7] and forms is the impetus for the present work.

1.3 Objective and scope

The main objective of the work presented in this thesis is to explore the nature of stress states at failure by adding the intermediate stress effect to experiments and investigating the accuracy of three failure criterion. A laboratory testing program was devised to study the mechanical properties of the Dunnville sandstone, to evaluate the existing failure criteria and to update the Paul-Mohr-Coulomb model for this rock. The following define the scope of this thesis:

1. Laboratory tests including unconfined compression tests, triaxial compression and extension tests are performed to characterize the rock mechanical properties such friction angle in compression and extension (ϕ_c and ϕ_e, respectively), Young's modulus (E) and Poisson's ratio (ν).

2. Most geotechnical engineering problems involves rocks subjected to a plane state of strain. It is particularly the case for tunnels, and other long structures with a constant cross-section and loaded in the plane of the cross-section [4]. A true-triaxial device is used to simulate a plane strain condition by where the minor principal stress (σ_3) is maintained at a desired target value and the intermediate stress (σ_2) is increased to develop a condition where $\Delta_{\epsilon_2} = 0$ and hence a plane strain condition is simulated.

3. A true triaxial device is used to develop a stress path to failure where the mean stress is kept constant during the deviatoric loading stage by decreasing the intermediate principal stress (σ_2) as failure is approached.

4. The test results from this thesis and those reported in literature used to evaluate the failure criteria available in the published literature.

5. The test results and a database of available tests will be used to calibrate the model parameters for a Paul-Mohr-Coulomb nonlinear failure criterion which considers the effect of intermediate principal stress.

This project addresses the need of an accurate representation of rock response by bringing new experimental conditions to rock testing, and by investigating a promising failure criterion through the analysis of a large database of experimentation results.

1.4 Thesis organization

This thesis is organized through the following layout.

Chapter 2 presents a review of three most widely used failure criteria through their formulation in four different coordinates systems, namely, Mohr-Coulomb, Hoek-Brown and Paul-Mohr-Coulomb. The following representations were chosen: (p-q) plane, (σ_1-σ_3) plane, as well as the π-plane and the (σ_1-σ_2-σ_3) space. The two last systems are linked as the π-plane is a plane perpendicular to the hydrostatic axis ($\sigma_1 = \sigma_2 = \sigma_3$) . Particular attention is given to the Paul-Mohr-Coulomb criterion, for which the fitting planes construction is detailed.

Dunnville Sandstone is the chosen test material for the experiment performed in this work. Chapter 3 introduces the rock geologic history as well as its mineralogy, and present procedures and results of initial experiments performed. A detailed description of uniaxial compression tests and conventional triaxial tests is provided.

Chapter 4 reviews the theoretical background on multiaxial and particularly "true-triaxial" experiments performed during this study. It is followed by a detailed presentation of the

Plane-Strain Apparatus and specimen preparation. Finally, the end of the chapter focuses on the procedures and results of plane strain and constant mean stress tests performed.

In Chapter 5, a complete analysis of the experiment results is presented. The new test data and the existing data from published literature are used to evaluate existing failure criteria, and to calibrate the Paul-Mohr-Coulomb failure criterion.

Finally, Chapter 6 conclude this thesis by summarizing the most important findings of this work.

2 Failure criteria

Failure criteria aim to describe in the most accurate way rock failure. The most successful criteria are a usually a generalization of experiments results, from a combination of axisymmetric and multi-axial tests. Indeed, failure criteria are a theoretical conjecture aimed to describe what is observed from material behavior. In this chapter, a presentation of the mathematical formulation of selected criteria is provided. The theory presented is based on the work of Labuz (2018) [1] and Folta (2016) [2], in which detailed descriptions of the failure criteria can be found.

2.1 Background on failure criteria

Failure criteria are a theoretical derivation of a fundamental mathematical function that describe rock failure:

$$f\left(\sigma_{xx}, \sigma_{yy}, \sigma_{zz}, \sigma_{xy}, \sigma_{yz}, \sigma_{zx}\right) = \text{ constant} \tag{2.1}$$

This function is expressed in terms of σ_{ij} the stresses acting on the rock. Equation 2.1 can be simplified in the case of iso

tropic material analysis. Indeed, the isotropic rock strength properties are the same in all directions, which leads to a directional independence of the stress state. The fundamental function can then be written as follow:

$$f\left(\sigma_{I}, \sigma_{II}, \sigma_{III}\right) = \text{ constant} \tag{2.2}$$

σ_I, σ_{II} and σ_{III} being the three principal stress acting on the rock, respectively major, intermediate and minor stress.

In order to emphasize on the directional independence of the stress state, the failure criteria can be formulated within the framework of the stress invariants. The fundamental mathematical formulation then becomes:

$$f\left(I_I, J_{II}, J_{III}\right) = \text{ constant} \tag{2.3}$$

$I_I$is the first invariant of the stress tensor σ_{ij} and J_{II}, J_{III} the second and third invariants of the deviatoric stress tensor :

$$I_1 = \sigma_I + \sigma_{II} + \sigma_{III} \tag{2.4}$$

$$J_2 = \frac{1}{6}\left[(\sigma_I - \sigma_{II})^2 + (\sigma_{II} - \sigma_{III})^2 + (\sigma_{III} - \sigma_I)^2\right] \tag{2.5}$$

$$J_2 = \left(\sigma_I - p\right)\left(\sigma_{II} - p\right)\left(\sigma_{III} - p\right) \tag{2.6}$$

From these invariants, three others can be defined, and will be used in this thesis: the mean stress p , the deviatoric stress q and the Lodge angle θ . Failure criteria are then described by:

$$f(p, q, \theta) = \text{constant} \tag{2.7}$$

$$p = \frac{I_1}{3} = \frac{\sigma_I + \sigma_M + \sigma_{III}}{3} \tag{2.8}$$

$$q = \sqrt{3J_2} = \frac{1}{6}\sqrt{\left[(\sigma_I - \sigma_{II})^2 + (\sigma_{II} - \sigma_{III})^2 + (\sigma_{III} - \sigma_I)^2\right]} \tag{2.9}$$

$$\theta = \frac{1}{3}\arccos\left(\frac{3\sqrt{3}}{2}\frac{J_3}{J_2^{3/2}}\right) = \arctan\left[\frac{\sqrt{3}\,(\sigma_M - \sigma_M)}{2\sigma_I - \sigma_{II} - \sigma_{MI}}\right] \tag{2.10}$$

The Lodge angle is a measure of the stress state: $0° \leq \theta \leq 60°$, particularly $\theta = 0°$ for axisymmetric compression $\sigma_{II} = \sigma_{III}$ and $\theta = 60°$ in the case of axisymmetric extension ($\sigma_{II} = \sigma_I$).

Equations 2.2, 2.3 and 2.7 unveils the three-dimensional nature of the failure envelop and consequently of failure criteria. Indeed, depending on the state of stress ordering, failure criteria describe six planes, or failure surfaces, in a three-dimensional $\sigma_1 - \sigma_2 - \sigma_3$ space: (i) $\sigma_1 \geq \sigma_2 \geq \sigma_3$, (ii) $\sigma_2 \geq \sigma_1 \geq \sigma_3$, (iii) $\sigma_2 \geq \sigma_3 \geq \sigma_1$, (iv) $\sigma_3 \geq \sigma_2 \geq \sigma_1$,(v) $\sigma_3 \geq \sigma_1 \geq \sigma_2$, (vi) $\sigma_1 \geq \sigma_3 \geq \sigma_1$. For instance, a linear criterion, written in terms of the three principal stresses, shows a pyramidal failure envelop of which the planes have a common vertex V_0 , the theoretical isotropic tensile strength, on the tension side of the space. This example is presented in Fig 2.1a.

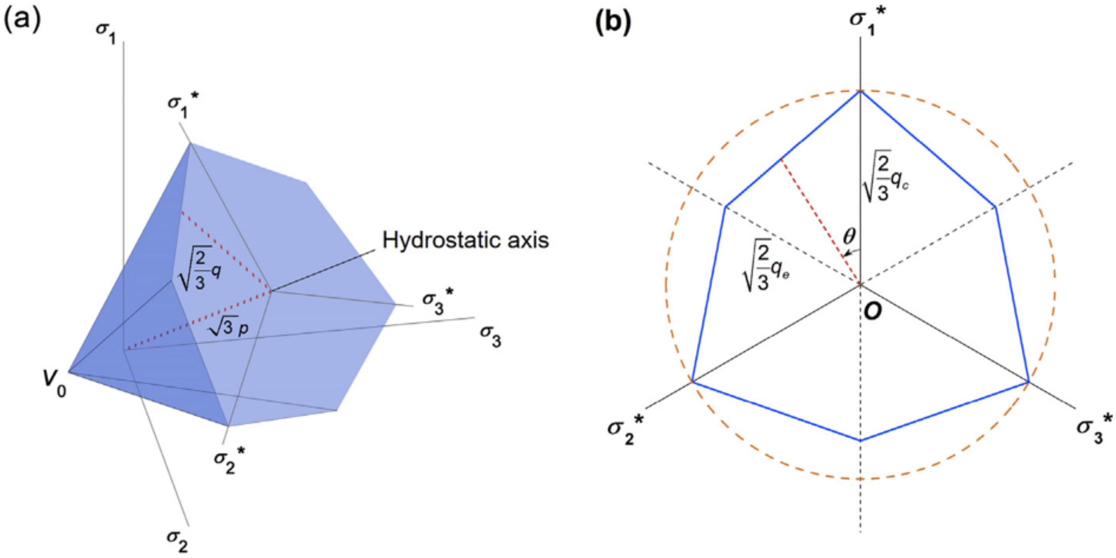

Figure 2.1: Failure surface in (a) the principal stress space and (b) the π-plane [1, Labuz 2018]

However, although the three-dimensional representation of the failure envelop is the most complete, it is not the most practical to use and to show. Therefore, two-dimensional coordinates systems are preferred, as the $(\sigma_3 - \sigma_1)$plane, the $(p - q)$ plane and the π-plane.

The π-plane. is a section of the failure envelop in the principal stress space, perpendicular to the hydrostatic axis. It is also called the equipressure plane, as the mean stress is constant over the plane. Moreover, the axes $(\sigma_1^*, \sigma_2^*, \sigma_3^*)$ are the projection of the coordinate axis on the π-plane (cf. 2.1b.). Each point on in the principal stress space can be represented in polar coordinates in this plane. As the mean stress is constant over the π-plane, the point is at a distance r from the origin of the hydrostatic axis and oriented at the Lodge angle θ from the σ_1^* axis. Then the principal coordinates of the same point on the π-plane can be written as:

$$\sigma_1 = p + \frac{\sqrt{6}}{3} r \cos(\theta) \tag{2.11}$$

$$\sigma_2 = p + \frac{\sqrt{6}}{3} r \sin\left(\frac{\pi}{6} + \theta\right) \tag{2.12}$$

$$\sigma_3 = p + \frac{\sqrt{6}}{3} r \sin\left(\frac{\pi}{6} - \theta\right) \tag{2.13}$$

In the next sections, selected failure criteria will be presented along with their formulation in each coordinates system.

2.2 Mohr-Coulomb criterion

The Mohr-Coulomb failure criterion (MC) is the most popular and widely used criterion. In its original formulation, it describes the shear strength of a material as a function of the normal stress σ , and two material parameters known as the internal failure angle θ and the cohesion c :

$$\tau = \sigma \tan\phi + c \tag{2.14}$$

This criterion was developed considering failure of isotropic materials without taking into account the intermediate stress effect. It can be written in terms of the major and minor stresses:

$$\tau = \frac{\sigma_I - \sigma_{III}}{2} \cos\phi \tag{2.15}$$

$$\sigma = \frac{\sigma_I + \sigma_{III}}{2} - \frac{\sigma_I - \sigma_{III}}{2} \sin\phi \tag{2.16}$$

Then in its final form:

$$\sigma_I = \frac{1+\sin\phi}{1-\sin\phi}\sigma_{III} + \frac{2c\cos\phi}{1-\sin\phi} \tag{2.17}$$

or

$$\sigma_I = K_p \sigma_{III} + C_0 \tag{2.18}$$

where K_p is the slope of the failure surface in $(\sigma_3 - \sigma_1)$plane and C_0 is the uniaxial compression strength of the rock.

2.2.1 Mohr-Coulomb in the $(\sigma_3 - \sigma_1)$ plane

Fig 2.2 present the graphical construction of MC envelop in the $(\sigma_3 - \sigma_1)$ plane. The common vertex of the failure surfaces in extension and compression can be expressed using $\sigma_I = \sigma_{III} = -V_0$:

$$V_0 = \frac{C_0}{K_p - 1} \tag{2.19}$$

As MC doesn't take into account the intermediate stress effect, it can only be representative of

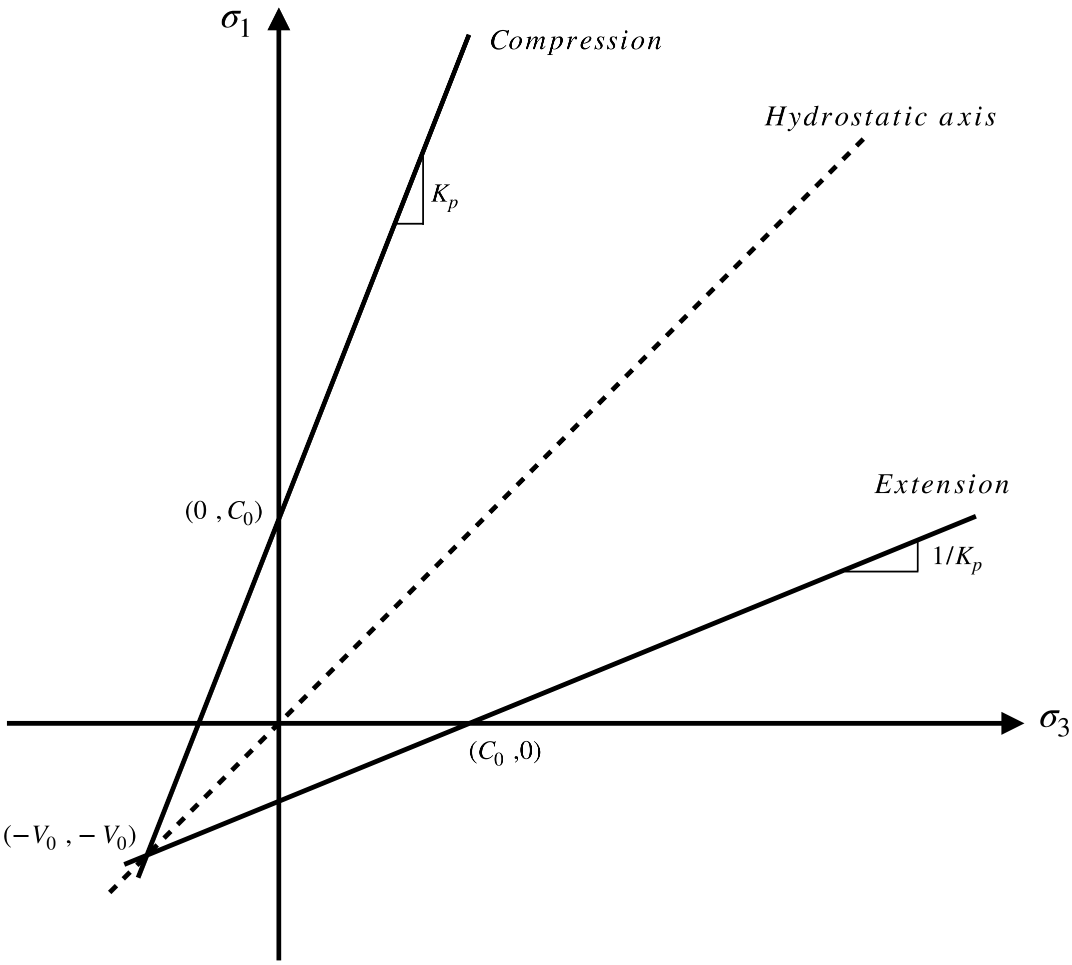

Figure 2.2: Mohr-Coulomb criterion failure surface in $(\sigma_3 - \sigma_1)$ plane

data from conventional triaxial tests which are defined by:

Conventional Triaxial Compression (CTC):

$$\sigma_I = \sigma_1 = \sigma_a$$
$$\sigma_{III} = \sigma_3 = \sigma_r$$
$$\sigma_{II} = \sigma_{III} = \sigma_3 = \sigma_r$$

Conventional Triaxial Extension (CTE):

$$\sigma_I = \sigma_3 = \sigma_r$$
$$\sigma_{III} = \sigma_1 = \sigma_a$$
$$\sigma_{II} = \sigma_I = \sigma_3 = \sigma_r$$

2.2.2 Mohr-Coulomb in the $(p-q)$ plane

The following development of the MC criterion is presented for CTC and can be adapted to CTE stress definition. Following CTC stress path, Equations 2.8 and 2.9 can be written as:

$$p = \frac{\sigma_a + 2\sigma_r}{2} \tag{2.20}$$
$$q = \sigma_a - \sigma_r \tag{2.21}$$

By rearranging Equation 2.17 and including the CTC conditions, MC criterion becomes:

$$\sigma_a - \sigma_r = ()\sigma_a + 2\sigma_r)\sin\phi + 2\cos\phi \tag{2.22}$$

Next equation is obtained by expanding and substituting Equation 2.20 and 2.20 in 2.22:

$$q(3-\sin\phi) = 6p\sin\phi + 6\cos\phi \tag{2.23}$$

Finally, the MC failure surface formulation in the plane is defined by Equation 2.24 for CTC and Equation 2.25 for CTE:

$$q = \frac{6\sin\phi}{3-\sin\phi}p + \frac{6\mathrm{ccos}\phi}{3-\sin\phi} \tag{2.24}$$

$$q = \frac{6\sin\phi}{3+\sin\phi}p + \frac{6c\cos\phi}{3+\sin\phi} \tag{2.25}$$

or in the condensed form:

$$q = m_{c,e}p + b_{c,e} \tag{2.26}$$

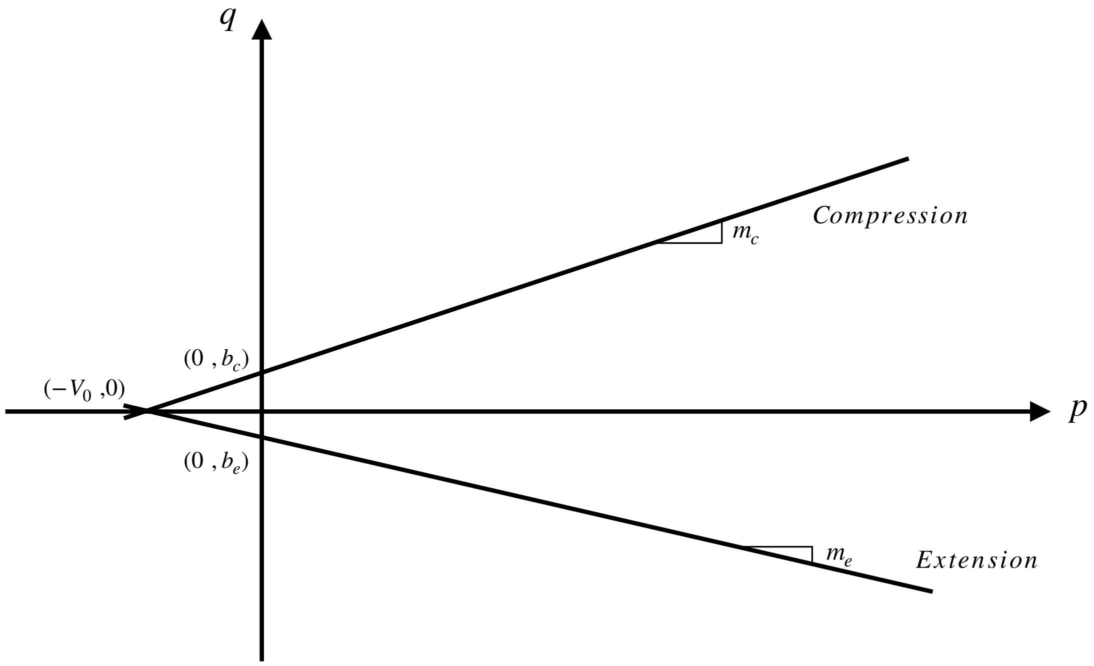

Figure 2.3: Schematic representation of Mohr-Coulomb criterion failure surface in $(p-s)$plane

where c and e defines m and b for compression or extension surfaces:

$$m_c = \frac{6\sin\phi}{3-\sin\phi} \tag{2.27}$$

$$m_e = \frac{6\sin\phi}{3+\sin\phi} \tag{2.28}$$

$$b_c = \frac{6c\cos\phi}{3-\sin\phi} \tag{2.29}$$

$$b_e = \frac{6c\cos\phi}{3+\sin\phi} \tag{2.30}$$

Fig. 2.3 present the graphical construction of the failure surfaces in the $(p-q)$plane. In order to distinguish compression from extension data, the failure surface in extension is showed using a negative deviatoric stress $-q$.

2.2.3 Mohr-Coulomb in the π-plane

The Mohr-Coulomb failure envelop in the π-plane is presented in Fig 2.4. The failure surfaces can be obtained by inserting Equation 2.11 and 2.13 in the criterion formulation defined by 2.18.

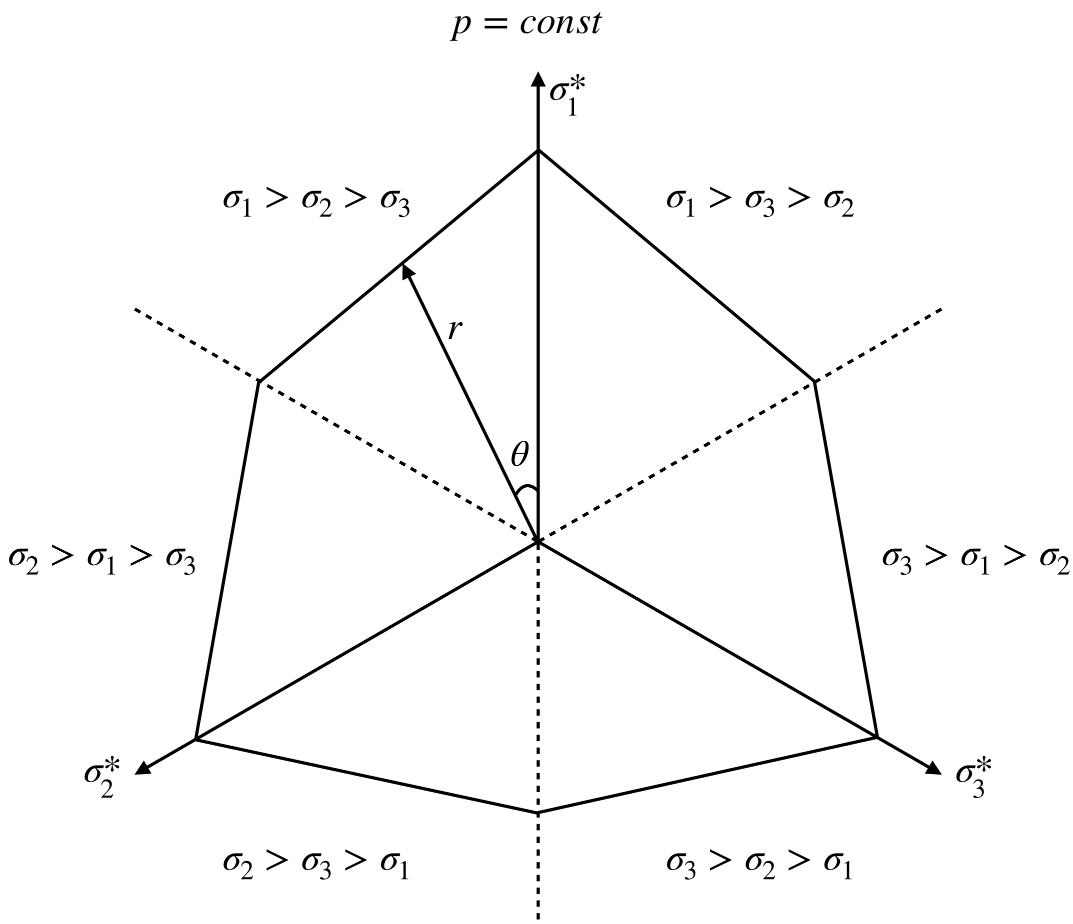

Figure 2.4: Schematic representation of Mohr-Coulomb criterion failure surface in πplane

2.3 Hoek-Brown criterion

The Hoek-Brown (HB) criterion is a non-linear criterion for isotropic rocks that doesn't take into account the intermediate stress effect. The empirical relationship developed between the principal stresses can be written as follow:

$$\sigma_I = \sigma_{III} + C_0 \sqrt{m \frac{\sigma_{III}}{C_0} + s} \tag{2.31}$$

Hoek and Brown (1980) [9] define m and s are constant depending on the rock properties. The constant s characterize the initial state of the tested rock: for intact rock $s = 1.0$. This value will be considered in the next developments. The strength parameter m is an empirical fitting parameter chosen depending on the rock type.

2.3.1 Hoek-Brown in the $(\sigma_3 - \sigma_1)$ plane

For conventional triaxial compression, the conditions presented in section 2.2.2 can be inserted in Equation 2.31 to obtain the criterion formulation in terms of the axial and radial stresses:

$$\sigma_1 = \sigma_3 + C_0\sqrt{m\frac{\sigma_1}{C_0} + 1} \tag{2.32}$$

Similarly, the formulation for conventional triaxial extension is written as:

$$\sigma_1 = \sigma_3 - \frac{\sqrt{4mC_0\sigma_3 + m^2C_0^2 + 4C_0^2} - mC_0}{2} \tag{2.33}$$

From Equation 2.32, the theoretical isotropic tensile strength V_0 can be expressed as a function of the uniaxial compression strength C_0, using : $\sigma_a = \sigma_r = -V_0$:

$$V_0 = \frac{C_0}{m} \tag{2.34}$$

Fig. 2.5 present the HB failure surfaces in the $(\sigma_3 - \sigma_1)$ plane.

2.3.2 Hoek-Brown in the $(p - q)$ plane

HB criterion can be expressed with the stress invariants and . By rearranging Equation 2.31 the formulation become:

$$(\sigma_I - \sigma_{III})^2 = C_0^2\left(m\frac{\sigma_{II}}{C_0} + s\right) \tag{2.35}$$

By rearranging and inserting p and q in Equation 2.35 (2.31), implicit formulation for CTC and CTE are obtained. Equation 2.36 for compression and 2.37 for extension describe HB criterion after solving roots of the implicit expressions:

$$q = \frac{1}{6}\left(\pm\sqrt{C_0}\sqrt{C_0m^2 + 36C_0 + 36mp} - C_0m\right) \tag{2.36}$$

$$q = \frac{1}{3}(\pm\sqrt{C_0^2m^2 + 9C_0^2 + 9C_0mp + C_0m}) \tag{2.37}$$

The HB criterion surface fitting in the plane is presented in Fig 2.6, where the positive root of Equation 2.36 and the negative root of Equation 2.37 are considered.

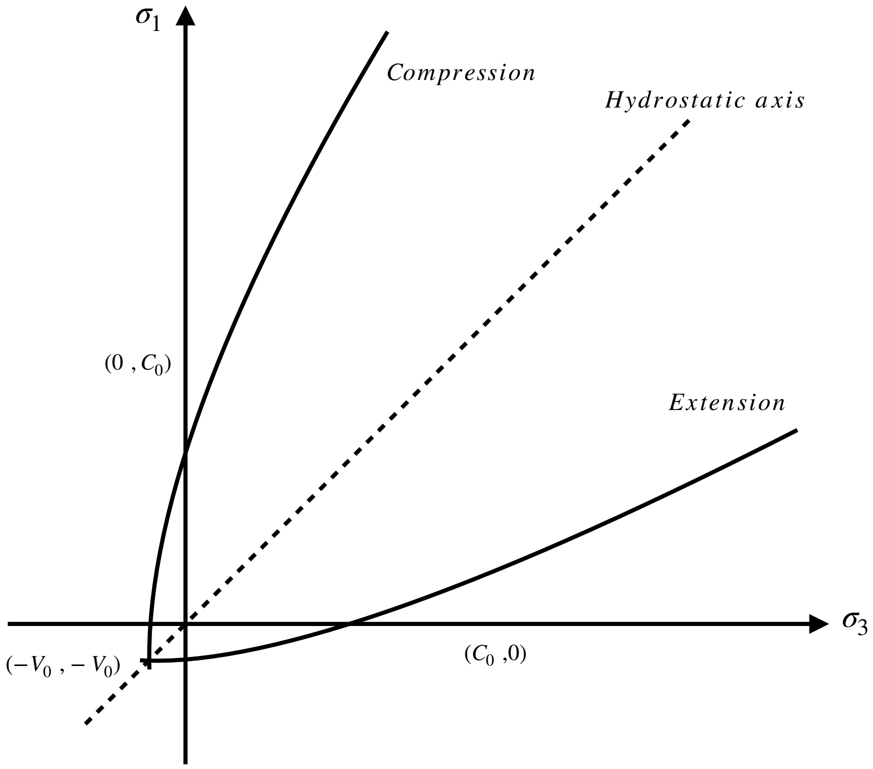

Figure 2.5: Schematic representation of Hoek-Brown criterion failure surface in $(\sigma_3 - \sigma_1)$ plane.

2.3.3 Hoek-Brown in the π plane

The Hoek-Brown failure envelop in the -plane is presented in Fig 2.7 The failure surfaces can be obtained by inserting Equation 2.11 (2.11) and 2.13 (2.13) in the criterion formulation defined by 2.31. In Fig 7, the surfaces are exaggerated to show the non-linearity of the criterion.

2.4 Paul-Mohr-Coulomb criterion

The Paul-Mohr-Coulomb criterion (PMC) is a linear criterion formulated in terms of the three principal stresses. Unlike the Mohr-Coulomb and Hoek-Brown, PMC is representative of all multi-axial experiments. Its formulation is based on the one developed by Mohr-Coulomb, for which the intermediate stress effect is added [7, Paul (1968)]).

PMC failure criterion have the following general expression:

$$A\sigma_I + B\sigma_{II} + C\sigma_{III} = 1 \tag{2.38}$$

The ordering of the A, B and C with the major, intermediate and minor stresses should be

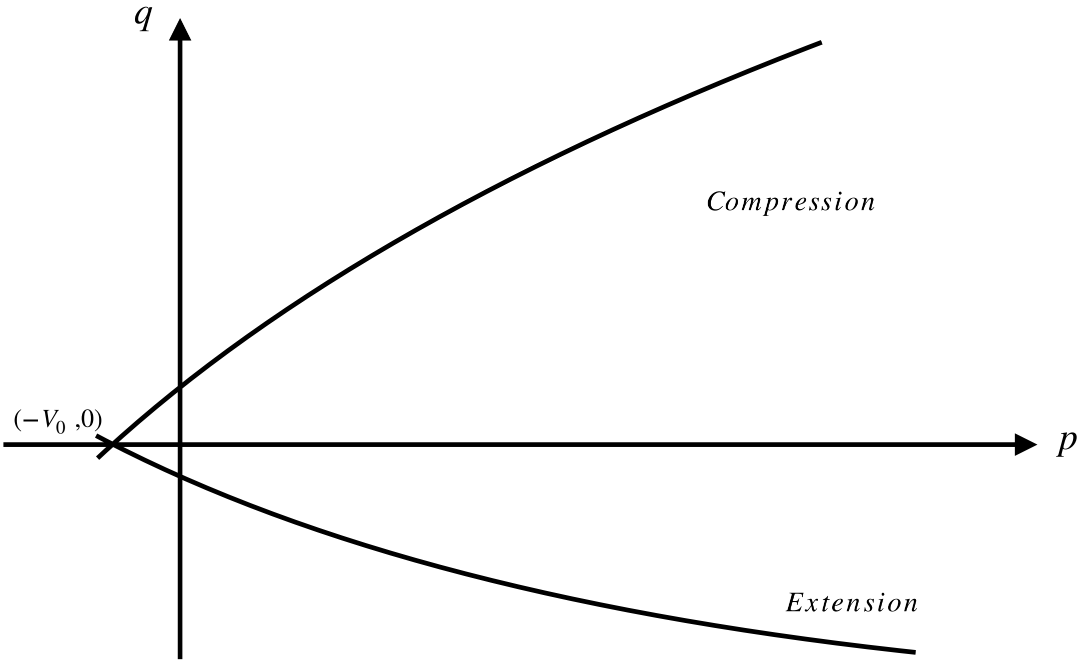

Figure 2.6: Schematic representation of Hoek-Brown criterion failure surface in $(p-q)$ plane.

kept as defined in Equation 2.38.

In their work, [8, Meyer and Labuz (2013)] provides the expression of the coefficient , and in terms of the rock properties:

$$A = \frac{1-\sin\phi_c}{2V_0\sin\ \phi_c} \tag{2.39}$$

$$B = \frac{\sin\phi_c - \sin\phi_e}{2V_0\sin\ \phi_e\sin\ \phi_c} \tag{2.40}$$

$$C = \frac{-1+\sin\phi_e}{2V_0\sin\ \phi_e} \tag{2.41}$$

$$\tag{2.42}$$

Equation 2.38 can therefore be written in its complete form as follow:

$$\sigma_I\left[\frac{1-\sin\phi_c}{2V_0\sin\phi_C}\right]+\sigma_I\left[\frac{\sin\phi_c-\sin\phi_e}{2V_0\sin\phi_e\sin\phi_C}\right]+\sigma_{III}\left[\frac{-1+\sin\phi_e}{2V_0\sin\phi_e}\right]=1 \tag{2.43}$$

PMC refines failure criterion definition by considering different values of the rock properties. It is shown in Equation 2.43 by the subscripts c and e, defining the variables for compression or extension.

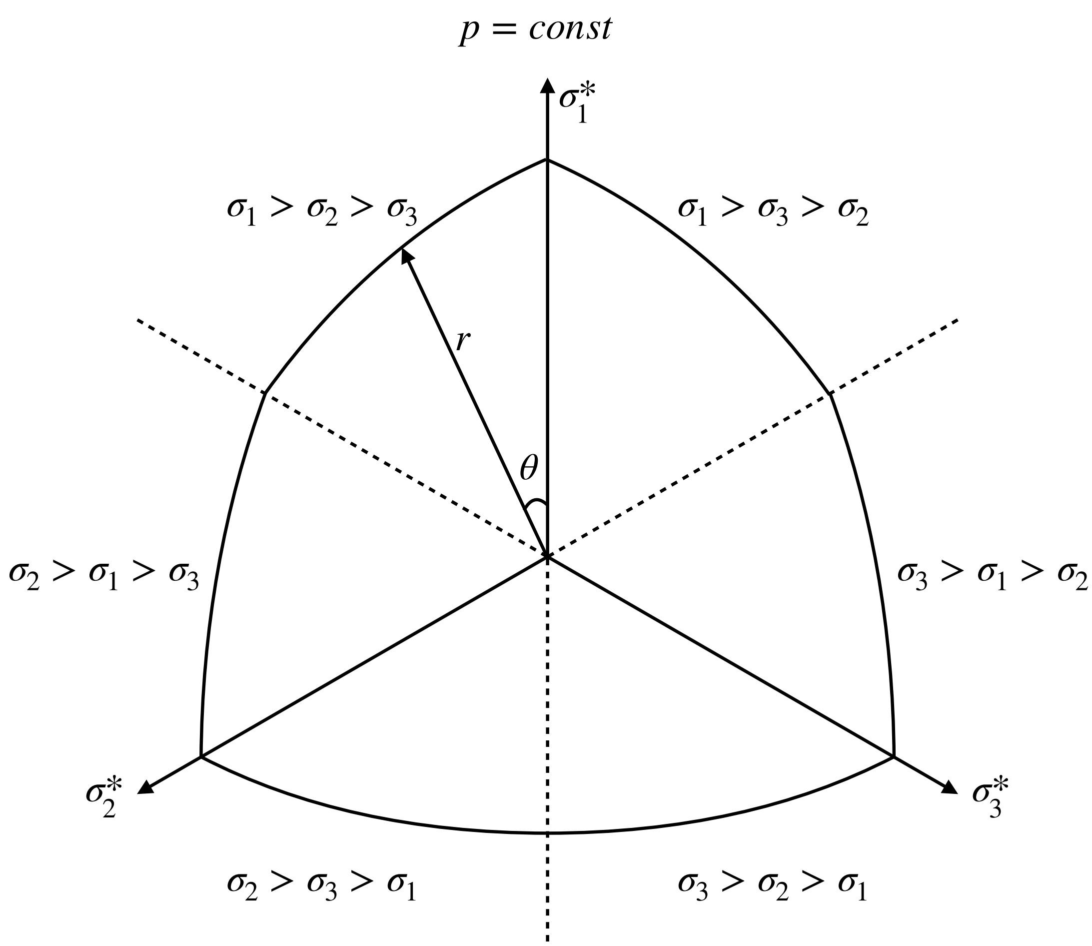

Figure 2.7: Schematic representation of Hoek-Brown criterion failure surface in π plane.

2.4.1 Paul-Mohr-Coulomb in the $(\sigma_3 - \sigma_1)$ plane

Paul-Mohr-Coulomb is based on the Mohr-Coulomb criterion, therefore its expression in the $(\sigma_3 - \sigma_1)$plane is an adjustment of Equation 2.43 considering different friction angles and cohesion for compression and extension conditions:

$$\sigma_I = M_{c,e}\sigma_{III} + Cc, e \tag{2.44}$$

Where:

$$M_{c,e} = \frac{1 + \sin\phi_{c,e}}{1 - \sin\phi_{c,e}} \tag{2.45}$$

$$C_{c,e} = \frac{2c_{c,e}\cos\phi_{c,e}}{1 - \sin\phi_{c,e}} \tag{2.46}$$

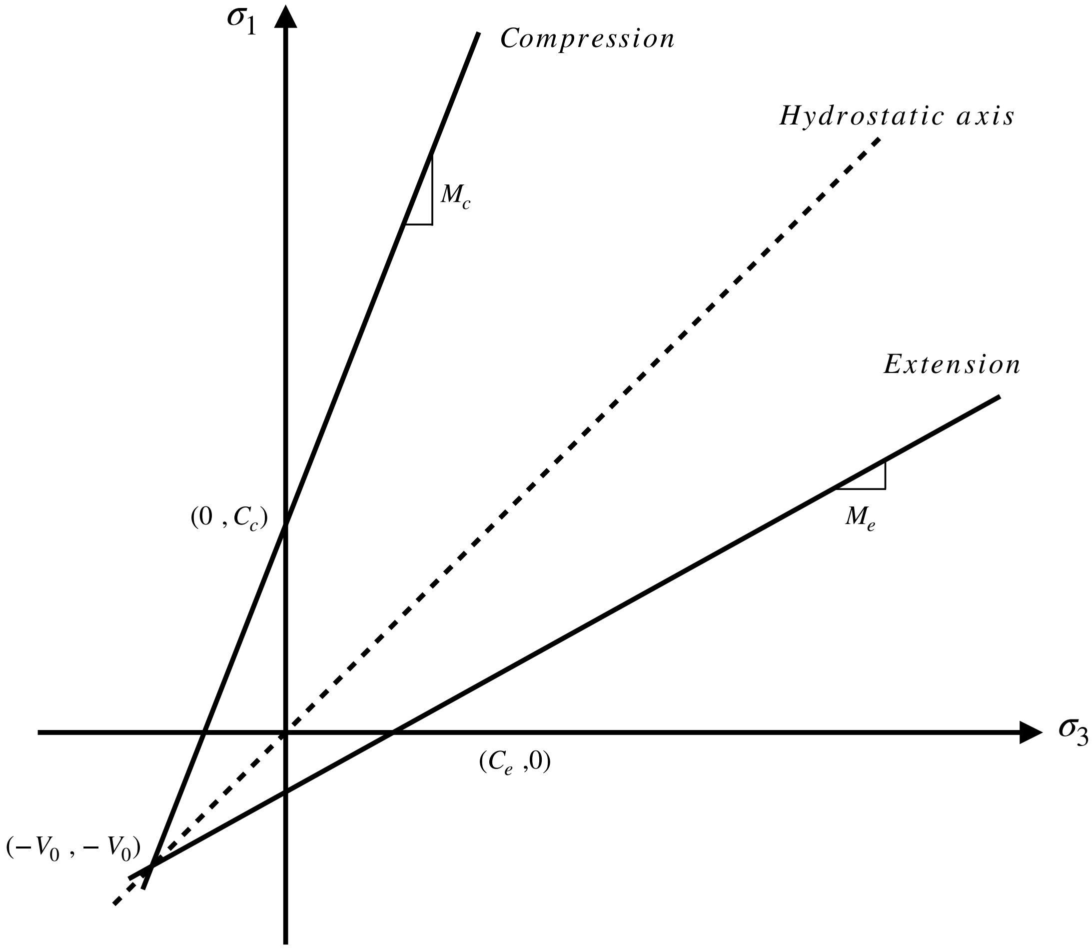

Figure 2.8: Schematic representation of Paul-Mohr-Coulomb criterion failure surface in $(\sigma_3 - \sigma_1)$ plane.

PMC failure surfaces in $(\sigma_3 - \sigma_1)$ plane are presented in Fig. 2.8. As the friction angle and the cohesion for compression and extension are non-equal, PMC isn't symmetrical over the hydrostatic axis. The computation V_0 of will be discussed in section 2.4.3.

2.4.2 Paul-Mohr-Coulomb in the $(p - q)$ plane

To represent PMC in the $(p - q)$ plane, an adjusted version of Equations 2.24 and 2.25 defined for MC can be used:

$$q = \frac{6\sin\phi_c}{3-\sin\phi_c}p + \frac{6c_c\cos\phi_c}{3-\sin\phi_c} \tag{2.47}$$

$$q = \frac{6\sin\phi_e}{3+\sin\phi_e}p + \frac{6c_e\cos\phi_e}{3+\sin\phi_e} \tag{2.48}$$

or in the simplifies form:

$$q = m_{c,e} p + b_{c,e} \tag{2.49}$$

where the coefficients $m_{c,e}$ and $b_{c,e}$ are defined as follow:

$$m_c = \frac{6 \sin \phi_c}{3 - \sin \phi_c} \quad \text{and} \quad m_e = \frac{6 \sin \phi_e}{3 + \sin \phi_e} \tag{2.50}$$

$$b_c = \frac{6 c_c \cos \phi_c}{3 - \sin \phi_c} \quad \text{and} \quad b_e = \frac{6 c_e \cos \phi_e}{3 + \sin \phi_e} \tag{2.51}$$

The same sketch of the failure surface as presented in Fig. 2.3 for Mohr-Coulomb can be used to represent Paul-Mohr-Coulomb criterion. The only difference is the non-equal values of the friction angles and cohesions in the computation of $m_{c,e}$ and $b_{c,e}$.

2.4.3 Paul-Mohr-Coulomb fitting

Failure criterion are conjectural. They try to provide a mathematical formulation of rock behavior based on experiments. However, the results obtained from them aren't direct measurements of the friction angle or cohesion, they give the state of stress at failure. The rock properties should then be computed from these stresses.

Failure criterion fitting consist in the computation of the rock properties (V_0, ϕ, c) from a mathematical formulation of the criterion written in terms of the three principal stresses. Labuz (2018) [1] and Folta (2016) [10] provide detailed mathematical derivation of Equations 2.11 - 2.13 that leads to the expression of Paul-Mohr-Coulomb failure criterion in terms of the stress invariants p, q and θ.

The final formulation is given by Equation 2.52:

$$q \cos(\phi) = \frac{b_c}{V_0} p + k \sin(\phi) q + b_c \tag{2.52}$$

where:

$$k = \frac{1 - 2\alpha}{\sqrt{3}} \tag{2.53}$$

$$\alpha = \frac{b_c}{b_e} \tag{2.54}$$

Each data point i from a conventional triaxial or multi-axial experiment is defined by a trio of (p_i, q_i, θ_i) values. Therefore, for one tested rock, Equation 2.52 describes a system of linear equations. This system has m equations, with m being the number of experiments performed on the considered rock. Equation 2.52 can also be written as a matrix equation of type $Ax = b$:

$$\begin{bmatrix} q_1 \cos(\theta_1) \\ \cdots \\ q_m \cos(\theta_m) \end{bmatrix} = \begin{bmatrix} p_1 & q_1 \sin\theta_1 & 1 \\ \cdots & \cdots & \cdots \\ p_m & q_m \sin\theta_m & 1 \end{bmatrix} \begin{bmatrix} b_c / V_0 \\ k \\ b_c \end{bmatrix} \tag{2.55}$$

with A a m-by-3 matrix, b a m-row vector and x a 3-row vector.

From the system defined in Equation 2.55, b_c , k and V_0 and can be determined. k and b_c are given by the second and third row of parameter vector x, V_0 and the extension parameter b_e are computed as follow:

$$V_0 = \frac{b_c}{x_1} \tag{2.56}$$

$$b_e = \frac{2b_c}{(1 - \sqrt{3}k)} \tag{2.57}$$

The rock parameters can now be defined by solving Equations for 2.47 and 2.48 for $q(p = -V_0) = 0$:

$$\sin\phi_c = \frac{3b_c}{6V_0 + b_c} \tag{2.58}$$

$$\sin\phi_e = \frac{3b_e}{6V_0 - b_e} \tag{2.59}$$

and $q(p = 0) = b_{c,e}$:

$$c_c = \frac{b_c \left(3 - \sin\phi_c\right)}{6\cos\phi_c} \tag{2.60}$$

$$c_e = \frac{b_e \left(3 + \sin\phi_e\right)}{6\cos\phi_e} \tag{2.61}$$

3 Dunnville sandstone characterization

This chapter presents a summary of geology, mineralogical composition and strength properties of Dunnville Sandstone. The results of simple tests such as uniaxial compression test and drained conventional triaxial tests on dry specimens are discussed and analyzed.

3.1 Geology, mineralogy and properties of the Dunnville sandstone

In this study, Dunnville sandstone was selected for the laboratory experiments due to its availability, known strength properties and its isotropic behavior at relatively high confining stresses. Indeed, previous experiments on Dunnville Sandstone showed an isotropic behavior under different conditions of triaxial testing [2]. The following paragraphs provide a short summary of geological and mineralogical properties of Dunnville sandstone.

3.1.1 Geological history

Dunnville sandstone comes from Dunnville, in western Wisconsin. The rock quarry is located in a valley at the intersection of the Chippewa river and one of its affluent. Dunnville sandstone constituent materials were deposited during the Cambrian period when Wisconsin was submerged several times by a sea, enabling the deposition of a large amount of sediments. The consolidation and compaction of the deposited materials by glaciers during the Pleistocene Epoch geological time and the subsequent removal of ice due to melting and rise in ambient temperatures led to the development of highly over-consolidated sedimentary rocks in the region (i.e., Dunnville sandstone). Dunnville sandstone is a member of the Elk Mount Formation and particularly the Eau Claire group [11].

3.1.2 Mineralogy

Dunnville Sandstone is composed of 90% of medium-grained quartz and a small amount of cementitious material and may be referred to as a quartz arenite. Other minerals are readily

Figure 3.1: Dunnville sandstone mineralogy

noticeable such as orange beds of alkali feldspars and biotite grains (Fig. 3.1). The elongated biotite crystals are disparately distributed in the rock matrix and oriented parallel to the bedding. The mineralogical composition of Dunnville sandstone performed by American Engineering Testing is summarized in Table 3.1 [2]. Dunnville sandstone is a highly porous and permeable rock, with a porosity of 29-30% [2].

Mineral	Volume [%]
Quartz	90-95
Alkali Feldspar	2-5
Biotite	2-5
Plagioclase	Trace -1
Muscovite	Trace
Clinozoisite	Trace
Zircon	Trace
Hematite	Trace
Iron-oxide	1-2

Table 3.1: Mineralogy of Dunnville Sandstone [2]

The dry density and the P-Wave velocity through the rock were measured for all specimens tested in this study. The dry density ρ is approximately 1910 ± 30 kg/m^3 and the P-wave velocity VP is 1825 ± 124 m/s . The wave travel time for evaluation of the P-wave velocity was measured perpendicular to the bedding planes in the tested specimens for uniaxial compression and drained conventional triaxial tests.

3.2 Uniaxial compression test

One uniaxial compression test was performed on Dunnville Sandstone, in order to determine Young's modulus E_i and the unconfined compressive strength C_o. These parameters are essential to understand the behavior of the rock and are used for the analysis of behavior in subsequent chapters.

3.2.1 Specimen preparation

A cylindrical specimen was already available from previous experiments. It was ground to ensure the ends were perpendicular to the specimen axis and dried prior to test in accordance with the ISRM suggested methods [12] and ASTM standard [13] [4]. A detailed description of the specimen preparation procedure will be presented in section 3.3.2. This specimen respected the standard dimensions for a uniaxial test (i.e. $h \approx 2d$) with the following characteristics: $h = 95.70$ mm, $d = 50.76$ mm. Following Labuz and Bridell (1993) [5], stearic acid was applied to the specimen ends to reduce end friction and thereby to minimize the end effects.

3.2.2 Procedure

The test was performed using a 1 MN MTS closed loop servo-hydraulic load frame (MTS System Corporation). The uniaxial compression test was stroke controlled to avoid sudden failure of the rock where a displacement rate of 0.001 mm s^{-1} was used. The displacement of the load frame and the force applied to the specimen was recorded during the test.

A small seating load of 1-2 kN was applied before the test initiated to ensure adequate contact between the loading platens and the specimen. The axial load was then increased until the achievement of 50% of the expected uniaxial compressive strength C_o of the rock following by unloading to 1-2 kN. The axial load was then increased until failure of the rock specimen was achieved. The test was continued until the load decreased to 75% of C_o. This loading-unloading cycle is used to determine the Young's modulus E_i of the rock after specimen displacements were corrected for the machine displacement.

For this test, the following stress path is considered:

$$\sigma_1 = \sigma_a \text{ with } \sigma_a > 0 \tag{3.1}$$

$$\sigma_2 = \sigma_3 = \sigma_r \text{ with } \sigma_r = 0 \tag{3.2}$$

3.2.3 Results

From the recorded axial displacement and force, the axial stress and the axial strain could be computed:

$$\sigma_a = \frac{F_a}{A} \tag{3.3}$$
$$\epsilon_a = \frac{u}{h} \tag{3.4}$$

Where:

σ_a : axial stress [MPa]

ϵ_a : axial strain [-]

$A = \frac{d\pi^2}{4}$: cross section area of the cylindrical specimen [mm^2]

F_a : axial load applied through the load frame [N]

u : axial displacement corrected for machine displacement [mm]

h length of the specimen [mm]

Fig 3.2 present the stress-strain plot obtained from the uniaxial compression test. The uniaxial compressive strength of the rock specimen is calculated as:

$$C_o = \frac{F_{\text{peak}}}{A} = \sigma_{a,\text{peak}} = 29.83\,\text{MPa} \tag{3.5}$$

The Young's Modulus of the rock is computed using the loading-unloading cycle:

$$E = \frac{\Delta\sigma}{\Delta\epsilon} = 5860\,\text{MPa} \tag{3.6}$$

Fig 3.3 presents the specimen after the test. The failed specimen showed a failure surface with a conical shape at 63°.

3.3 Conventional Triaxial tests

Dunnville sandstone shear strength was determined using conventional triaxial tests (CT). Two types of CT tests were performed, namely, the conventional triaxial compression (CTC) and the conventional triaxial extension (CTE). For these tests, two of the principal stresses of the stress state are equal. The state of stress of the rock specimen is then simplified to a combination of the axial stress σ_a and the radial stress σ_r.

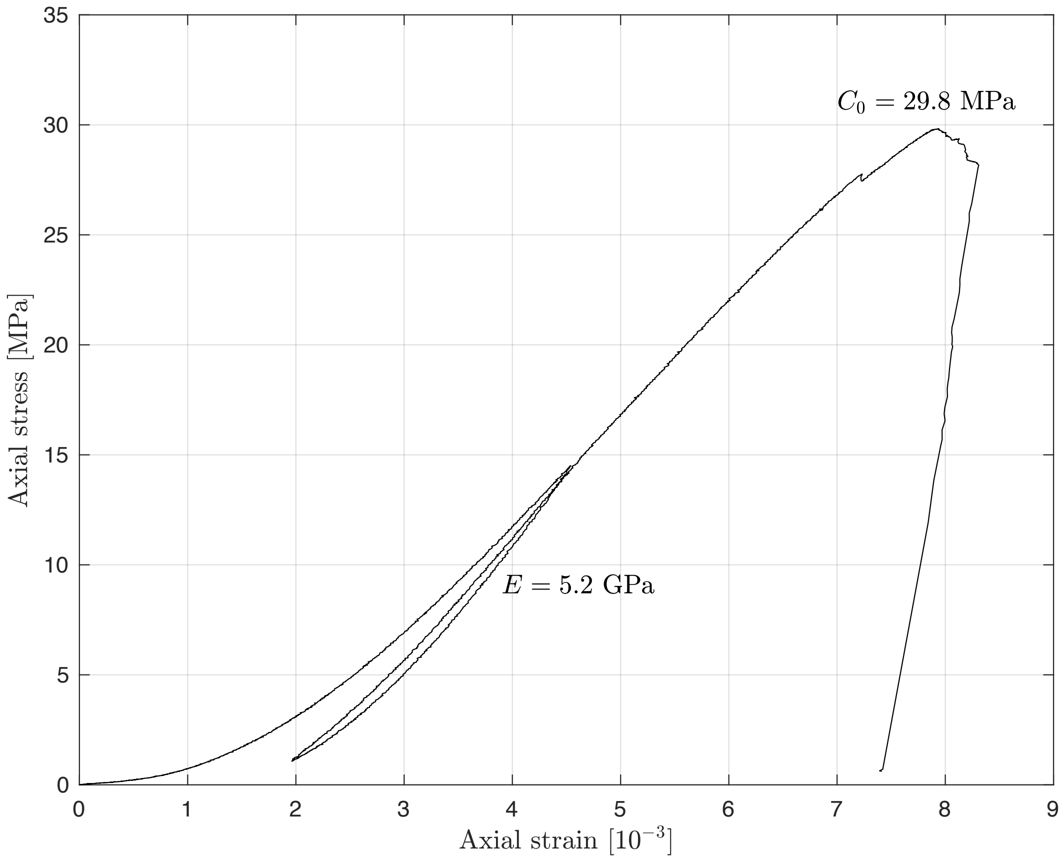

Figure 3.2: Stress and Strain relationship for the uniaxial compression test

3.3.1 Hoek-Franklin cell

A Hoek -Franklin pressure cell was used to perform the conventional triaxial tests [14]. The maximum capacity of the cell is 69 MPa and allows for the independent application of axial and radial stresses. The device is composed of a pressure vessel, a synthetic rubber membrane and two loading platens (Fig 3.4).

The radial stress was applied using a fluid pressure system where confinement is provided using hydraulic oil. The fluid pressure system is composed of a microcontroller and a screw-type hydraulic intensifier that allows for confining pressure to be held constant throughout the test. The axial load is applied through steel platens with a 1 MN MTS servo-hydraulic load frame (MTS System Corporation). The monitoring of the load frame and axial force measurement are done using a closed-looped and data acquisition system (Fig 3.5).

A rubber membrane was used to isolate the specimen and the loading platens from the confining fluid, and to allow for radial and axial stresses to be applied independently. The membranes used herein have an inner diameter of 32.0 mm and are 85.0 mm in height (Fig 3.6).

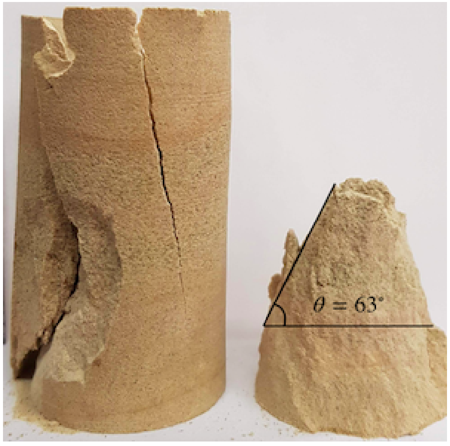

Figure 3.3: Stress and Strain relationship for the uniaxial compression test

3.3.2 Specimen preparation

Rock cores were obtained from a block of Dunnville sandstone. The specimens were prepared following ASTM Standard Practice D4543-19 [13]. In preparation of the test specimens, particular attention was given to (i) the straightness of the elements on the cylindrical surface, (ii) flatness of the end bearing surfaces and (iii) perpendicularity of the end surfaces with the respect to axis of the core. The following describes the procedure used in preparation of the specimens:

1. *Cutting and grinding of the end surfaces*: for the purpose of sealing, the specimen dimensions should match that of the Hoek-Franklin cell membrane. The core diameters ranged from 30.2 mm to 30.6 mm. The specimens were cut and ground to reach a height h of approximately 85.0 mm The specimens were cut using a saw table and ground using a diamond impregnated wheel. Finally, a precision table was used to ensure that specimen ends were perpendicular to the specimen axis. The final height h of the specimens ranged from 75.7 mm to 81.8 mm

2. *Drying*: all the specimens were oven dried at 150 °C for at least 24 hours before the tests to ensure drained conditions existed during the triaxial tests

3. *Minimizing end friction*: the ends and cylindrical surface of the specimens were coated with stearic acid [13]. This lubricant was used to reduce frictional effects between the membrane and the specimen.

In addition to standard geometrical preparation, one specimen (i.e. TC 9 at $\sigma_r = 5$ MPa) was equipped with a strain gages rosette where axial and transverse strains were measured (Fig 3.7). The procedure for the strain gages sets up had to be executed with much care to avoid damaging it. All the tools used in the process were cleaned with acid and neutralizer before touching the strain gage. Due to the high porosity of the Dunnville Sandstone, the surface of

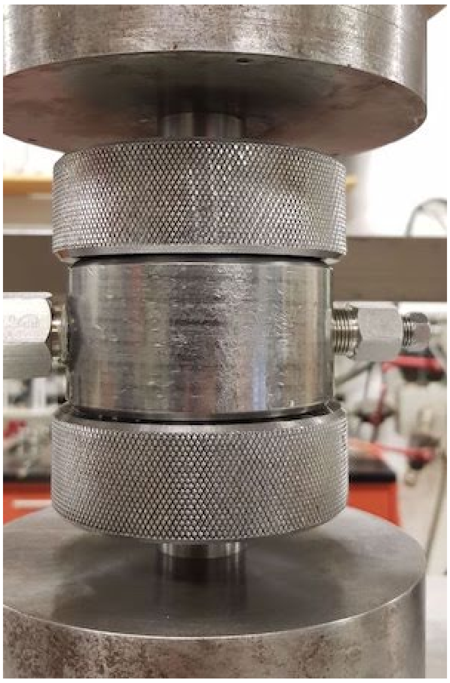

Figure 3.4: Hoek-Franklin cell

the rock had to be coated with the same epoxy that was used to attach the component. The surface of the specimen was then cleaned using xylene and the strain gage was attached using M-Bond 200 adhesive.

3.3.3 Conventional Triaxial Compression test

The following procedure was followed to setup and run the conventional triaxial compression tests:

1. The specimen was inserted in the Hoek-Franklin cell. The cell was held in a horizontal position and hydraulic oil was inserted to ensure no entrapped air existed in the annulus between the cell walls and the membrane.

2. The pressure cell-specimen-loading platen assembly was then placed inside the load frame and seating stress of $\sigma_a \approx 1\,\mathrm{MPa}$ was applied to the specimen to ensure adequate contact between the specimen and the platens. To ensure small deviatoric stresses, we also applied a $\sigma_r \approx 1\,\mathrm{MPa}$. It is noted that this condition corresponds to a hydrostatic stress state (i.e. $\sigma_a = \sigma_r = 1\,\mathrm{MPa}$).

3. The axial (σ_a) and radial (σ_r) stresses were then increased hydrostatically until the desired confining pressure (σ_r) was achieved. In so doing, a stress increment of ~5 MPa was consistently used.

Figure 3.5: Conventional triaxial test set up

4. Once the desired confining pressure (i.e., radial pressure σ_r) was reached, the deviatoric loading was initiated by maintaining the radial stresses (σ_r) while axial stresses (σ_a) were increased until failure was achieved. It is noted that all tests were stroke controlled where a displacement rate of 0.001 m s^{-1} was used. The stress path applied during the test can be summarized as follow:

$$\sigma_1 = \sigma_a \text{ with } \sigma_a > 0 \tag{3.7}$$

$$\sigma_2 = \sigma_3 = \sigma_r \text{ with } \sigma_r = 0 \tag{3.8}$$

$$\sigma_a > \sigma_r \tag{3.9}$$

σ_1, σ_2 and σ_3 are the principal stresses of the stress state; respectively major, intermediate and minor stress. The radial stress was kept constant at the desired confining pressure using the hydraulic intensifier, while the axial stress increased through the stroke of the load frame.

Figure 3.6: Membrane hosting the rock specimen in the Hoek-Franklin cell

3.3.4 Conventional Triaxial Compression test

The following procedure was followed to setup and run the conventional triaxial extension tests:

1. The same device and tests preparation, as the those previously explained for the conventional triaxial compression tests, were used for the conventional triaxial extension tests (i.e., see steps 1-3 in Section 3.3.3).

2. In a conventional triaxial extension test, however, the axial load is decreased as opposed to increasing the axial stress in triaxial compression tests.

3. This test was stroke controlled and a displacement rate of 0.001 $\mathrm{m\,s^{-1}}$ was used consistently. The radial stress was kept constant at the desired confining pressure using the hydraulic intensifier, while the axial stresses decreased through the displacement of the load frame. The stress path applied during the test can be summarized as follow:

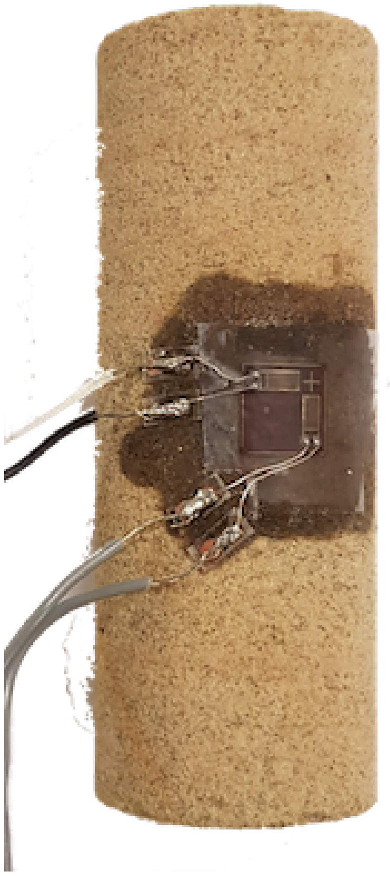

Figure 3.7: Strain Gage set up on a CTC specimen

$$\sigma_1 = \sigma_2 = \sigma_r \text{ with } \sigma_r = 0 \quad (3.10)$$

$$\sigma_3 = \sigma_a \text{ with } \sigma_a < 0 \quad (3.11)$$

$$\sigma_a < \sigma_r \quad (3.12)$$

σ_1, σ_2 and σ_3 re the principal stresses of the stress state; respectively major, intermediate and minor stress. The radial stress was kept constant at the desired confining pressure using the hydraulic intensifier, while the axial stress increased through the stroke of the load frame.

3.3.5 Tests results

Five conventional triaxial compression tests (i.e. σ_r = 5 MPa, 10 MPa, 20 MPa, 40 MPa and 60 MPa) and three conventional triaxial extension tests (i.e., σ_r = 35 MPa, 40 MPa and 60 MPa) were performed. The test results are summarized in Table 3.2 and the stress-strain relation-

Test	σ_1 [MPA]	σ_2 [MPA]	σ_3 [MPA]	p [MPA]	q [MPA]	θ [°]	E_i [MPA]
TC 9	49.43	5	5	19.81	44.43	0	5861
TC 0	61.43	10	10	27.95	51.43	0	6407
TC 5	91.08	20	20	44.72	71.08	0	7014
TC 8	127.3	40	40	65.73	87.30	0	6687
TC 10	151.1	60	60	88.12	91.10	0	6842
TE 3	35	35	3.96	24.64	31.08	60	7922
TE 1	40	40	4.50	27.89	36.34	60	8390
TE 2	60	60	9.68	43.01	50.98	60	8695

Table 3.2: Summary of CTC and CTE tests results

Segment	[°]	c[MPa]
5 – 10 MPa	30.73	9.67
10 – 20 MPa	29.37	10.42
20 – 40 MPa	14.41	23.6
40 – 60 MPa	4.72	36.94

Table 3.3: Mohr-Coulomb strength parameters for various stress regimes for Dunnville sandstone

ships for all tests are shown in Fig 3.8

Conventional triaxial tests

Stress vs. strain plot From 0 MPa to 20 MPa of confining stress, the rock is in the brittle domain as the axial stress is dropping after reaching its maximal strength. At higher confining pressures (i.e., $\sigma_r > 40$MPa and $\sigma_r < 60$MPa), however, rock is transitioning from a brittle to ductile response as represented by the post-peak drop in stresses as seen in Fig. 3.8. Finally, the rock shows a ductile behavior under a confining stress of 60 MPa, were the stress doesn't reach a peak value, but keep increasing as multiple failure surfaces are created.

Mohr circles plot The conventional triaxial compression results can also be presented using Mohr-Coulomb theory and particularly Mohr circles and their failure envelope. Fig. 3.9 presents the Mohr circles of the five CTC tests. This plot indicates that the failure envelop for Dunnville sandstone is stress dependent and cannot be represented using the Mohr-Coulomb linear failure envelop for the entire range of possible stress states. The nonlinear failure envelop, however, may be linearized over small stress intervals as shown in Fig 3.9. The corresponding Mohr-Coulomb strength parameters (i.e., friction angle ϕ and cohesion intercept c) are summarized in Table 3.3.

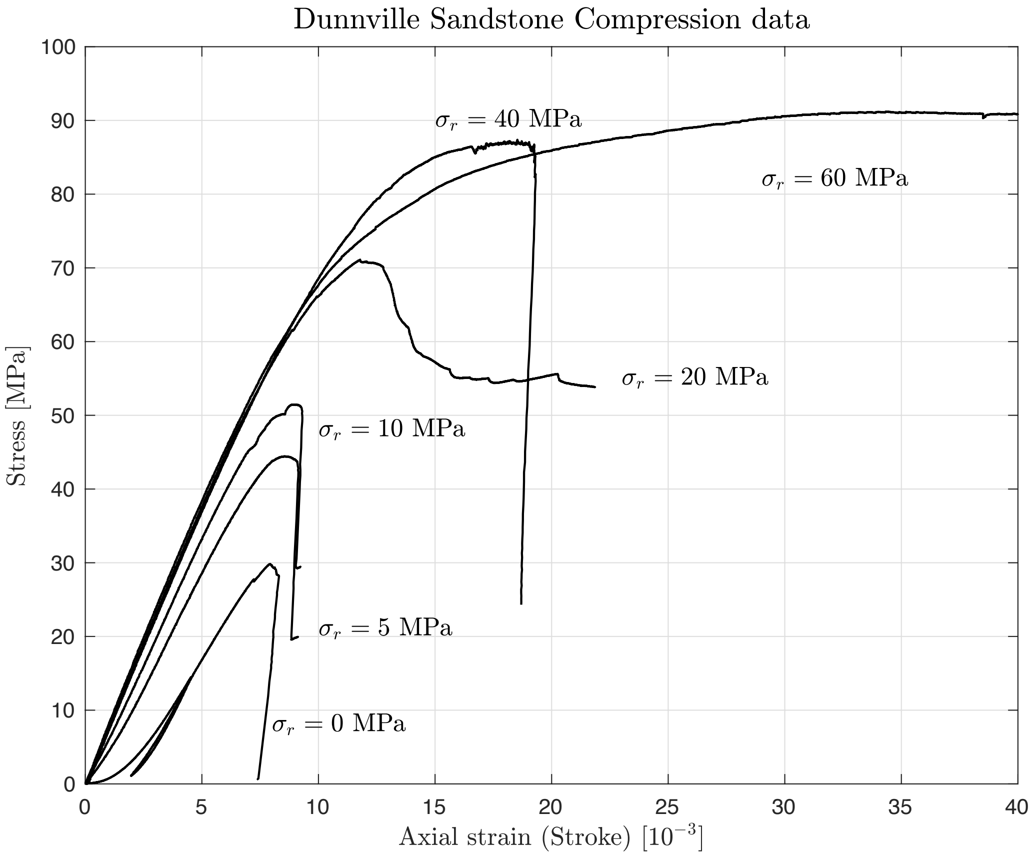

Figure 3.8: Summary of the stress-strain relationships for the triaxial compression and extension tests

Poisson's ratio The Poisson's ratio of Dunnville Sandstone was computed using the results of the axial and radial strains for specimen TC 9:

$$\nu = \frac{-\epsilon_{\text{radial}}}{\epsilon_{\text{axial}}} = 0.26 \tag{3.13}$$

Fig 3.10 shows a plot of the radial strain vs. the axial strain measured during the test.

Failure surfaces Table 3.4 presents pictures of the CTC tests specimens after failure, where failure surfaces are observable. For all the tests, the failure angle is about 60°, which correspond well to the theory associated with failure of isotropic rock under triaxial compression.

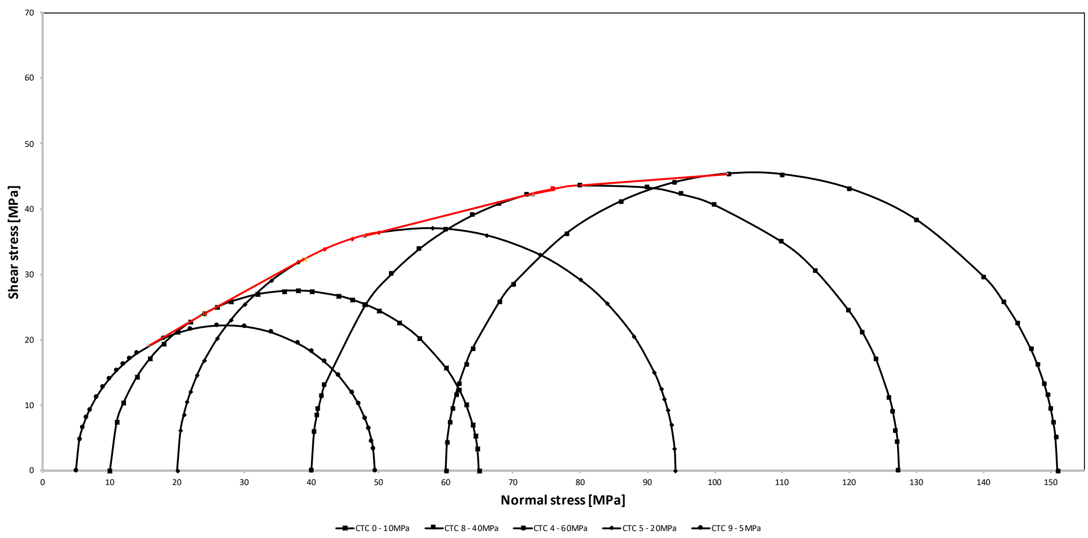

Figure 3.9: Mohr-Coulomb circles for the conventional triaxial compression tests.

Conventional triaxial tests

Stress vs. strain plot Fig 3.8 also presents the stress vs. strain curves for the extension tests. The axial stress in the figure represent the amount of axial stress that is removed from the stress state. In order to find the axial stress at failure, the following formula is used:

$$\sigma_{\text{failure}} = \sigma_{a,\text{removed}} - \sigma_r \tag{3.14}$$

The extension curves showed in the Fig. 3.8 present a sudden increase in axial stress followed by a constant axial stress. This behavior is due to the failure of the specimen and particularly to the dilatancy of the specimen on the failure surface. As the failure surface is formed, the radial stress is higher than the axial stress and the confining pressure pushes the specimen out of the cell. The increase in axial stress is due to type of test performed, which is under displacement control. The load frame is still moving at the same rate, but the specimen is moved up against the load cell at a higher displacement rate.

Failure surfaces Table 3.5 presents pictures of the CTE tests specimens after failure. From Mohr-Coulomb theory, the expected orientation of the failure surface for isotropic rocks under triaxial compression is horizontal. The tested specimen show failures surfaces close to horizontal. The observable variations for 35 MPa and 60 MPa come from the small anisotropy due to the rock bedding, as the angles correspond to the bedding angles.

$\sigma_r = 5\,\text{MPa}$	$\sigma_r = 10\,\text{MPa}$	$\sigma_r = 20\,\text{MPa}$	$\sigma_r = 40\,\text{MPa}$	$\sigma_r = 60\,\text{MPa}$
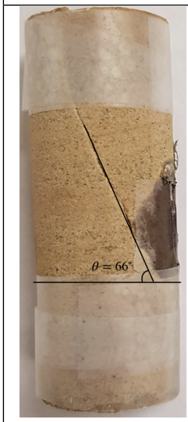	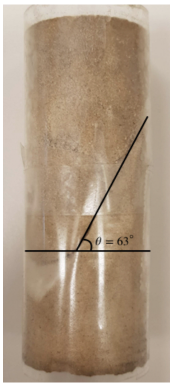	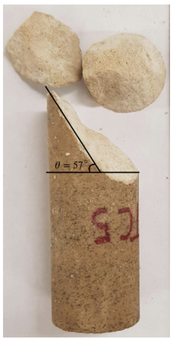		
$\theta = 66°$	$\theta = 63°$	$\theta = 57°$	$\theta = 58°$	$\theta = ?$

Table 3.4: Failure surfaces for conventional triaxial compression tests

$\sigma_r = 35\,\text{MPa}$	$\sigma_r = 40\,\text{MPa}$	$\sigma_r = 60\,\text{MPa}$
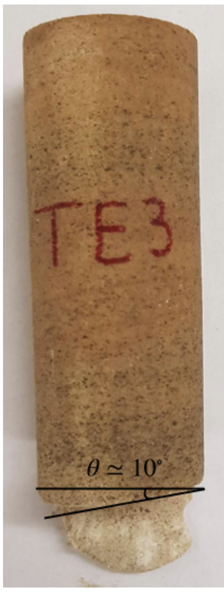	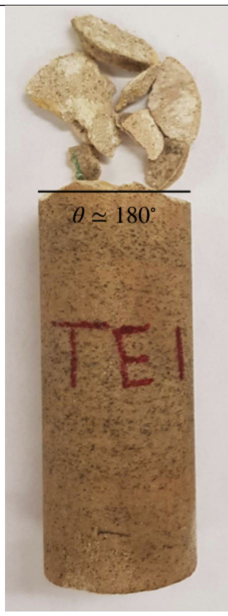	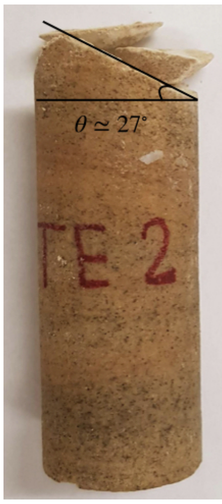
$\theta = 10°$	$\theta = 0°$	$\theta = 27°$

Table 3.5: Failure surfaces for conventional triaxial extension tests

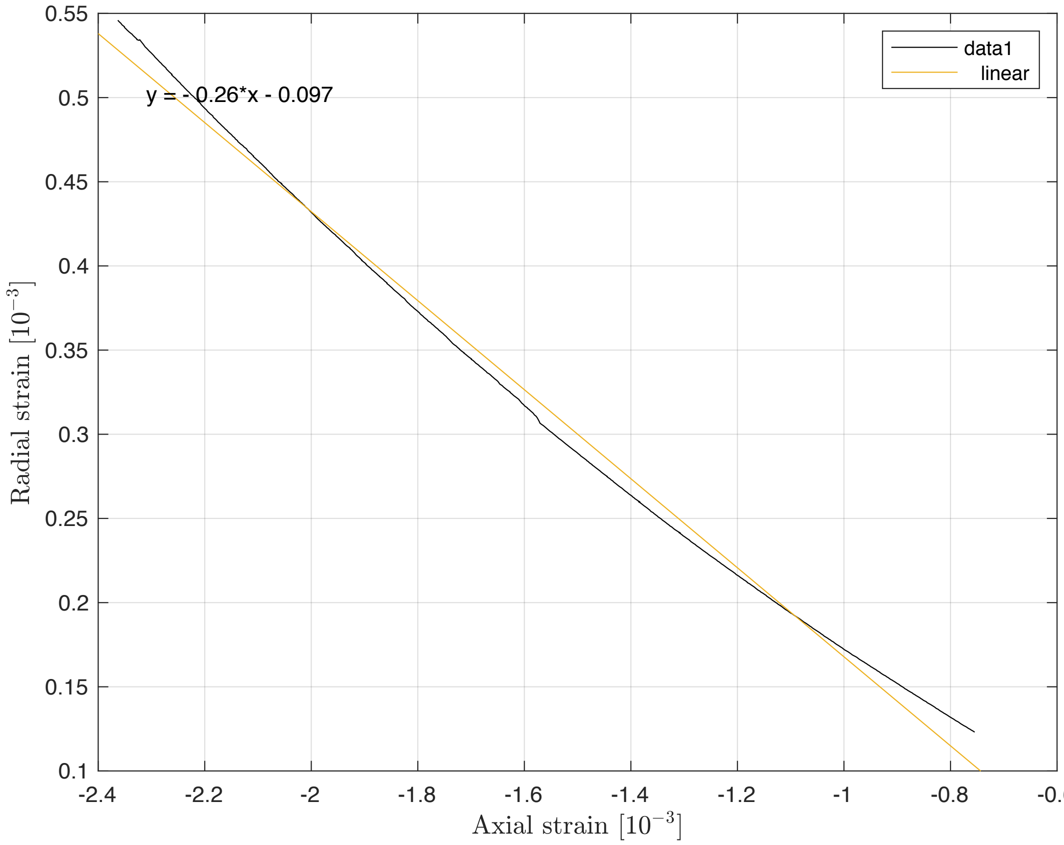

Figure 3.10: poisson

4 Multi axial experiments

The quest for a successful failure criterion requires experiments and particularly multi-axial testing [1] to be performed. They are needed to assess the intermediate principal stress effect and to enrich the experiments database used to calibrate failure criteria theories such as Paul-Mohr-Coulomb. This chapter presents the multi axial experiments performed for this study.

4.1 Introduction

The development of failure criteria requires a diversity of experiments to be the representative of the rock behavior. Axisymmetric or conventional triaxial experiments, presented in the previous chapter (cf. Chapter 3), are typical laboratory techniques performed as a first approach to determine strength parameters. However, although they are convenient to performed, they show limitations in their inability to independently apply the three principal stresses. To address this issue, multi axial experiments were developed with the aim to represent the in-situ state of stresses that rocks undergo during structural work, by creating “true-triaxial” testing conditions which can simulate various three-dimensional states of stress [1] .

In addition to the three-dimensional state of stress, most geotechnical engineering problems involves rocks subjected to a plane state of strain. It is particularly the case for tunnels, and other long structures with a constant cross-section and loaded in the plane of the cross-section [4]. Although this representation of the rock state is an accurate model of the reality, the condition is challenging to reproduce in experiments. Indeed, on top of independent application of the three principal stresses, the plane-strain condition requires a precise control of the strain in the intermediate stress direction, as it should be equal to zero for the duration of the test.

In this study, the Plane-Strain Apparatus developed by Labuz (1996) [5] was selected to perform the experiments on Dunnville Sandstone, as it enables to perform experiments that combines a three-dimensional stress state and a plane strain state of strain.

4.2 Plane-Strain Apparatus

The Plane-Strain Apparatus developed at the University of Minnesota enables independent application of the principal stresses, using a stiff biaxial frame to induce the intermediate stress through passive restraint [5]. Recent modifications of the device now enable control and monitoring of the three stresses, using hydraulic pistons [3].

4.2.1 Development of the apparatus

The Plane-Strain Apparatus (US Patent number 5 063 785), developed at the Laboratory of Rock Mechanics of University of Minnesota, was first designed based on a passive stiff frame concept. The device enabled testing of rock specimen under plane strain conditions with active application of the major and minor stresses, and passive restraint for the intermediate stress through the biaxial frame [5].

The apparatus was recently improved with the addition of two hydraulic pistons acting in the intermediate principal stress direction which enable the active application and control of major, intermediate and minor stresses [3]. This device allows failure surfaces to develop and propagate in an unrestricted manner, unlike conventional triaxial compression where the specimen is constrained by the apparatus. In short, the Plane-Strain Apparatus gives the possibility to simulate in-situ conditions of rock confinement underground by performing test on rock specimen under confined and plane-strain conditions.

4.2.2 Description of the apparatus

The apparatus can be defined as a pressure cell made of 4 components, each one related to a particular feature of the testing conditions [5, 3].

Base unit The base unit of the apparatus is equipped with high-pressure pass throughs designed to receive in-vessel instrumentation such as LVDTs (Linear Variable Differential Transformer), strain gages, and is made of an internal load cell where the specimen is placed. It is associated with displacement, strain and internal load measurements. Figure 4.1 shows the base unit and denotes its components.

Biaxial frame e biaxial frame was designed to bring maximum possible stiffness to the apparatus when it was used to apply passive restraint to the specimen. It is now hosting the hydraulic pistons, with a maximum capacity of 69 MPa, that directly induce the intermediate stress. The frame is placed on around the specimen so that the pistons are aligned with the lateral platens fixed to the specimen. Two holes were machined in the frame in order to allow a good placement of the lateral LVDTs. Figure 4.2 shows the biaxial frame and denotes its components.

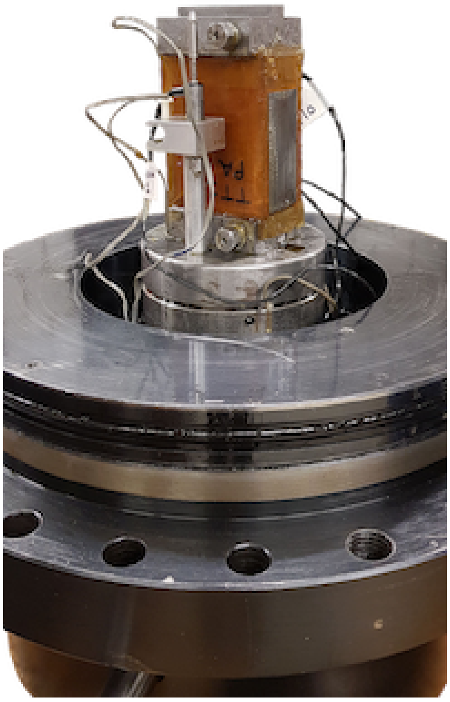

Figure 4.1: Base unit of the Plane-Strain Apparatus

Loading piston The loading piston assembly combines two features of the apparatus. It is used to apply the axial load to the specimen and enables the failure surface to develop and propagate freely in the minor stress direction. It is composed of a linear bearing, bolted to the bottom of the loading piston, which can slide over a trackway when failure surface propagates. The loading piston maximum capacity is 500 MPa. Figure 4.3 shows the loading piston assembly and denotes its components.

Pressure cell The four elements presented above are placed in a pressure cell designed to hold the pressurized fluid used to apply the minor stress. The top cap and base pot are bolted to a pressure vessel surrounding the apparatus. The pressure cell maximum capacity is 24 MPa. Figure 4.4 shows the pressure cell and denotes its components.

4.3 Specimen preparation

The concept of multi axial testing involves the use of a prismatic specimen. Indeed, in order to respect their independence, each of the three principal stresses have to be applied perpendicularly to the specimen surface. The specimen preparation included geometric adjustments, instrumentation with strain gages and jacketing.

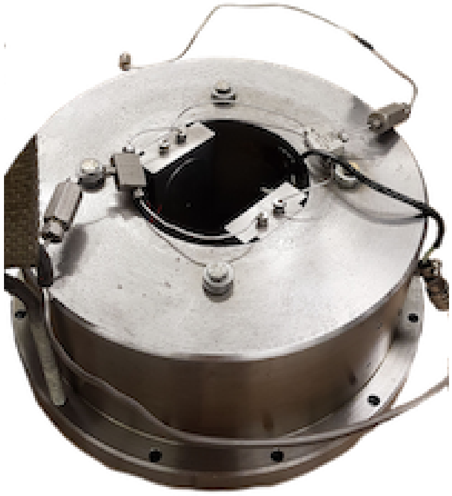

Figure 4.2: Biaxial Frame of the Plane-Strain Apparatus

4.3.1 Geometric preparation

The theoretical dimensions of the specimen used for true-triaxial testing in the Plane-Strain Apparatus are presented in the Figure 4.5.

Four prismatic specimens were obtained from a unique block of Dunnville sandstone to preserve identical properties among the experiments. In preparation of the test specimens, particular attention was given to:

i the straightness of the elements on the cylindrical surface,

ii flatness of the end bearing surfaces and

iii perpendicularity of the end surfaces with the respect to axis of the core.

In order to adjust the specimen dimensions and to ensure (i), (ii) and (iii), they were ground according with the ISRM suggested methods [12] and ASTM standard [13]. A detailed description of the specimen preparation procedure is presented in section 3.3. The final dimensions for the four specimens tested were: $h = (69 \pm 1)$ mm, $L = (60 \pm 1)$ mm, $b = (30.0 \pm 0.5)$ mm.

The true-triaxial experiments, in the Plane Strain Apparatus, are performed under drained conditions. After the geometry adjustment, the specimens were oven dried for 24 hours at 150 °C.

4.3.2 Specimen instrumentation

Strain measurements in the three principal directions are needed to analyze the behavior of the rock specimen during the experiment. These measurements were made using strain gages

Figure 4.3: Loading piston of the Plane-Strain Apparatus

as part of the instrumentation setup for multi axial tests.

One face of the specimens was equipped with a pair of strain gages made of one for axial strain and the other for transversal strain measurements. The set-up procedure is the same as the one described in section 3.3. Once the strain gages were fixed (24 hours of drying), the connector wires were soldered to them. Figure 4.6 shows the instrumentation of specimen “TT2”.

4.3.3 Jacketing

During an experiment in the Plane-Strain Apparatus, the specimen and the instrumentation are immersed in oil used to apply one of the lateral stresses. As the true-triaxial experiments were performed under drained conditions, the specimen needed to be dry (i.e. drained) for the duration of the test.

The specimen is protected from the oil by a polyurethane membrane that include the top, bottom and lateral platens in contact with the specimen (cf. Figure 4.7a). It is done to prevent any leakage of oil inside the sample that could lead to a loss of strength for the specimen, which makes it an important but also challenging step of the experiment setup. The following coating procedure was applied:

Figure 4.4: Pressure cell of the Plane-Strain Apparatus

1. The upper, lower and lateral platens were put in contact with the instrumented specimen and held together using clamps (cf. Figure 4.7b)

2. Each face of the specimen is covered with two layers polyurethane paste, each dried for 24 hours at room temperature

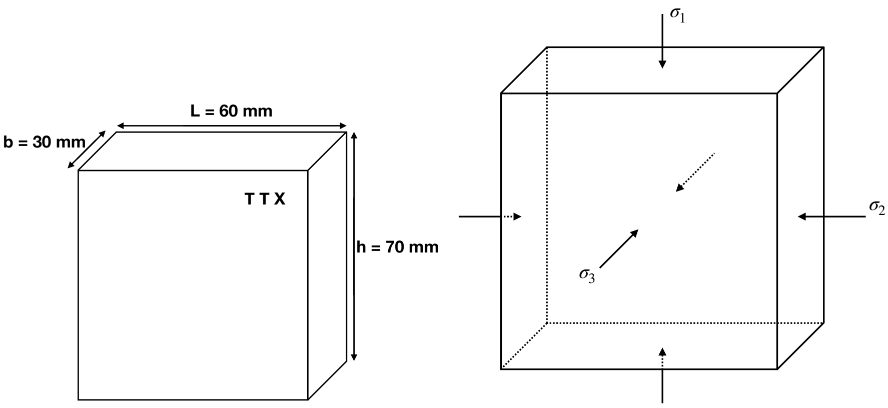

Figure 4.5: a. Specimen dimensions and b. loading directions

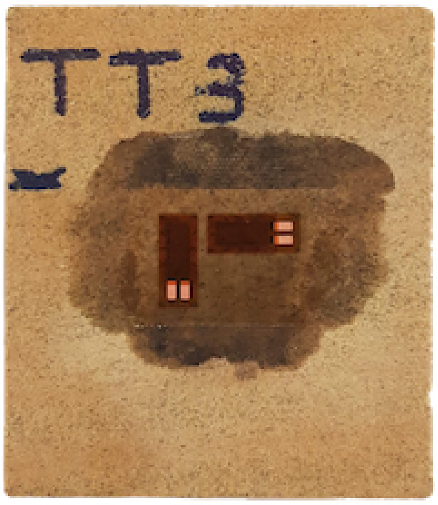

Figure 4.6: Specimen instrumented with axial and transversal strain gages

4.4 Experiments

Although the apparatus was designed about 30 years ago, the loading pistons were recently added to the biaxial frame. This new feature gave the possibility to explore new experiments conditions offered by the Plane-Strain Apparatus. Four tests were performed under different testing conditions and configuration of the equipment.

4.4.1 True-triaxial testing

Since the Plane-Strain Apparatus was improved with hydraulic pistons, several true triaxial experiments, particularly under constant mean stress conditions have been performed. However, none were done under plane strain conditions. One of this study objectives was to perform the first true triaxial experiment under plane strain condition in the Plane-Strain Apparatus.

Apparatus set-up

1. The specimen, coated with polyurethane, was placed on the internal load cell and the height of the vertical LVDTs was adjusted. The three LVDTs and the strain gages were connected to high-pressure pass throughs located on the base unit.

2. The biaxial frame was then placed on the base unit, around the specimen, and the loading piston assembly put on top of the specimen and adjusted so that it was centered with the base unit. A LVDT was then attached to the linear bearing (cf. Figure 4.8).

3. The pressure cell was placed around the previous assembly, bolted with the base unit and filled with oil.

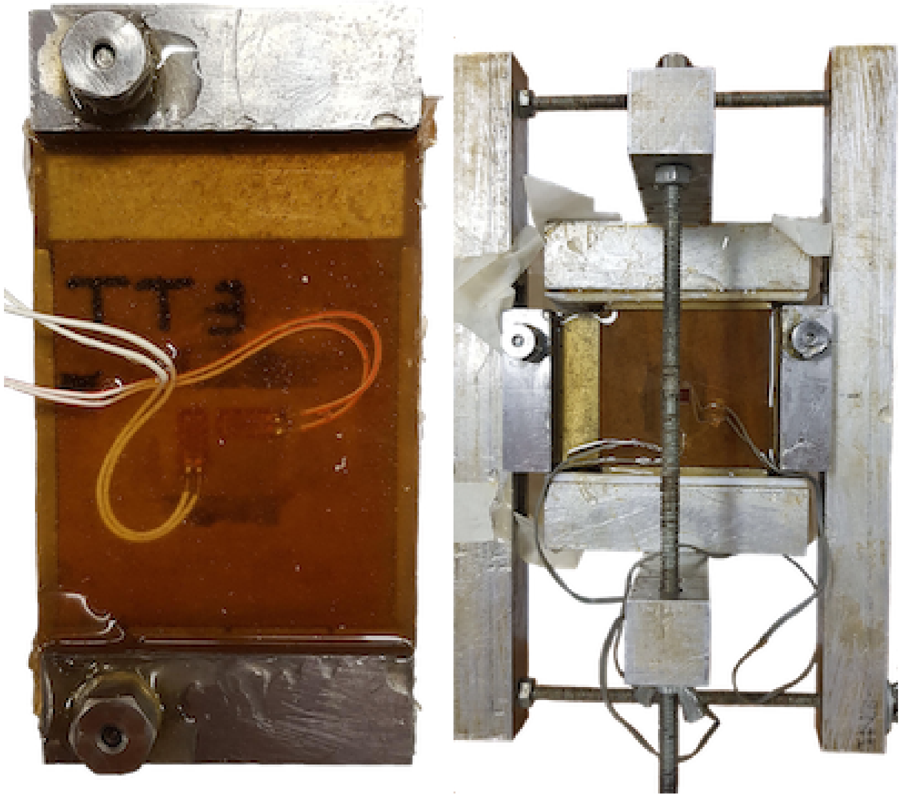

Figure 4.7: a) Jacketed specimen and b) coating set-up

4. Finally, the top cap was connected to the pistons' hydraulic circuit and bolted to the pressure cell.

Plane strain condition

The plane strain testing condition involves control of the strain in the intermediate stress direction. As the axial (i.e. major) stress increases until failure, the intermediate stress should constantly be adjusted during the test to keep the strain constant and equal to zero in its direction.

The following procedure was applied to perform the true-triaxial experiment under plane strain condition:

1. The Plane-Strain Apparatus was assembled, placed inside the MTS load frame the instrumentation was connected to the monitor.
2. The hydraulic intensifiers were connected to the pressure cell and the pistons. Each one was bled to ensure no entrapped air existed in the hydraulic circuit.

Figure 4.8: Apparatus set-up for the true-triaxial experiments

3. Seating stresses of $\sigma_1 = \sigma_2 \approx 1\,\text{MPa}$ were applied to the specimen to ensure adequate contact between the specimen and the platens. A $\sigma_3 \approx 1\,\text{MPa}$ was also applied to keep a small deviatoric stress. It is noted that this condition corresponds to a hydrostatic stress state (i.e., $\sigma_1 = \sigma_2 = \sigma_3 = 1\,\text{MPa}$).

4. The three principal stresses were then increased hydrostatically until the desired confining pressure (σ_3) was achieved. In so doing, a stress increment of ~2 MPa was consistently used. A small deviatoric stress of about 1 MPa was kept during the hydrostatic loading to ensure good contact between the platens and the specimen.

5. Once the desired confining pressure (i.e. minor stress σ_3) was reached, the deviatoric loading was initiated by maintaining the minor stresses (σ_3) constant while the major stress (σ_1) was increased until failure was achieved. The intermediate stress was manually applied and controlled so that the strain in the intermediate stress direction (ϵ_2) was kept constant and equal to zero during the test. The stress path applied during the

test can be summarized as follow:

$$\sigma_1 > 0$$
$$\sigma_3 = 0$$
$$\epsilon_2 = 0$$

he minor stress was applied using a fluid pressure system where confinement is provided using hydraulic oil. The fluid pressure system is composed of a microcontroller and a screw-type hydraulic intensifier that allows for confining pressure to be held constant throughout the test. A second hydraulic intensifier was used to apply the intermediate stress through the hydraulic pistons. The major stress was applied through the loading piston with a 1 MN MTS servo-hydraulic load frame (MTS System Corporation). The experiment was monitored using a closed-looped and data acquisition system.

During the test, the following measurements were recorded:

- Internal load applied to the specimen (Input: Internal load cell)
- Vertical displacement of the specimen (Input: LVDTs)
- Axial and transversal strain of the specimen (Input: Strain gages)
- Fluid pressure applied to the specimen (i.e. σ_3) (Input: Hydraulic intensifier)
- Fluid pressure applied to the pistons (i.e. σ_2) (Input: Hydraulic intensifier)
- Displacement of the linear bearing (LVDT)

It is noted that the test was stroke controlled using a displacement rate of $0.0005\,\mathrm{m\,s^{-1}}$ which was monitored from the average of the two vertical LVDTs measurements.

Constant mean stress condition

In order to compare the results given by the test described above, a true-triaxial experiment under constant mean stress condition was performed at a similar stress state as the one achieved at failure under plane strain condition.

The following procedure was applied:

1. The Plane-Strain Apparatus was assembled, placed inside the MTS load frame the instrumentation was connected to the monitor.

2. The hydraulic intensifiers were connected to the pressure cell and the pistons. Each one was bled to ensure no entrapped air existed in the hydraulic circuit.

3. Seating stresses of $\sigma_1 = \sigma_2 \approx 1\,\text{MPa}$ were applied to the specimen to ensure adequate contact between the specimen and the platens. A $\sigma_3 \approx 1\,\text{MPa}$ was also applied to keep a small deviatoric stress. It is noted that this condition corresponds to a hydrostatic stress state (i.e., $\sigma_1 = \sigma_2 = \sigma_3 = 1\,\text{MPa}$).

4. Hydrostatic loading phase: The three principal stresses were then increased hydrostatically until the desired confining pressure ($sigma_3$) was achieved. In so doing, a stress increment of ~2 MPa was consistently used. A small deviatoric stress of about 1 MPa was kept during the hydrostatic loading to ensure good contact between the platens and the specimen.

5. "Deviatoric" loading phase 1: Once the desired confining pressure (i.e. minor stress σ_3) was reached, the deviatoric loading was initiated by maintaining the minor stresses (σ_3) constant while the major (σ_1) and intermediate (σ_2) stresses were increased to the same value corresponding to the desired mean stress. The stress path applied during the phase can be summarized as follow:

$$\sigma_1 = \sigma_2 = \sigma_{1,2} \text{ with } \sigma_{1,2} = 0 \tag{4.1}$$

$$\Delta_3 = 0 \tag{4.2}$$

6. "Deviatoric" loading phase 2: Once the desired mean stress was reach, it was kept constant during the rest of the test. To do so, the minor stress was kept constant and the major and intermediate stresses followed $\Delta\sigma_1 = -\Delta\sigma_2$ until failure was achieved.

The lateral stresses were applied using two hydraulic intensifiers connected to the pressure vessel and the pistons. The major stress was applied through the loading piston with a 1 MN MTS servo-hydraulic load frame (MTS System Corporation). The experiment was monitored using a closed-looped and data acquisition system.

During the test, the following measurements were recorded:

- Internal load applied to the specimen (Input: Internal load cell)
- Vertical displacement of the specimen (Input: LVDTs)
- Axial and transversal strain of the specimen (Input: Strain gages)
- Fluid pressure applied to the specimen (i.e.) (Input: Hydraulic intensifier)
- Fluid pressure applied to the pistons (i.e.) (Input: Hydraulic intensifier)
- Displacement of the linear bearing (LVDT)

It is noted that the test was stroke controlled using a displacement rate of $0.0005\,\mathrm{m\,s^{-1}}$, which was monitored from the average of the two vertical LVDTs measurements.

4.4.2 “Un-conventional” triaxial compression experiment

One of the specimens prepared for an experiment under constant mean stress condition was too large to fit the biaxial frame. As the specimen preparation is time consuming, it was decided to modify the Plane-Strain Apparatus, by removing the biaxial frame, and to perform an “un-conventional” triaxial test on a prismatic specimen.

In this configuration, the apparatus preserved the base unit, the loading piston and the pressure cell. The axial (i.e. major) stress was still applied by the loading piston and the intermediate stress was induced through fluid pressure, equal to the minor stress. The stress state that undergoes the specimen during this experiment was similar to the one applied in conventional triaxial compression, hence the name given to the experiment (i.e. “un-conventional” triaxial compression).

In addition to the change in specimen geometry, this experiment brings a new feature to conventional triaxial compression testing, as it enables unrestricted development and propagation of the failure surface. Using this device to perform a “un-conventional” triaxial compression test was the opportunity to create new type of experiment that can bring more understanding to rock behavior at failure.

Apparatus set-up

For this experiment, the Plane-Strain Apparatus configuration was modified by removing the biaxial frame. In addition to the usual elements of the device, three steel cylinders equipped with threaded rod were placed between the base unit and the loading piston assembly (cf. Figure 3.9).

In the standard configuration of the device, the biaxial frame act as an emergency stopping block that protect the instrumentation below the loading piston, in case of a sudden drop of the assembly due to brittle failure of the specimen for example. However, in this “un-conventional” triaxial testing set-up, nothing stands between the base unit and the loading piston. The three cylinders were then added to the apparatus to replace the biaxial frame and avoid damaging the instrumentation around the specimen. Their height was adjusted in order to have a less than 5mm spacing with the loading piston, which correspond to the displacement range of the LVDTs placed next to the specimen.

As more space was available around the specimen, lateral LVDTs were also added the apparatus, to measure its displacement and strain in the minor stress direction.

Figure 4.9: Apparatus set-up for the “un-conventional” triaxial experiment

Procedure

The procedure defined for conventional triaxial compression in chapter 3 was followed for this experiment:

1. The Plane-Strain Apparatus was assembled and placed inside the MTS load frame.
2. A seating stress of $\sigma_a \approx 1\,\text{MPa}$ was applied to the specimen to ensure adequate contact between the specimen and the platens. To ensure small deviatoric stresses, we also applied a $\sigma_r \approx 1\,\text{MPa}$. It is noted that this condition corresponds to a hydrostatic stress state (i.e., $\sigma_r = \sigma_a \approx 1\,\text{MPa}$).
3. The axial (σ_a) and radial (σ_r) stresses were then increased hydrostatically until the desired confining pressure (σ_r) was achieved. In so doing, a stress increment of ~2 MPa was consistently used.
4. Once the desired confining pressure (i.e., radial stress σ_r) was reached, the deviatoric loading was initiated by maintaining the radial stresses (σ_r) constant while the axial

stress (σ_a) was increased until failure was achieved. The stress path applied during the test can be summarized as follow:

$$\sigma_1 = \sigma_a \text{ with } \sigma_a > 0 \tag{4.3}$$

$$\sigma_2 = \sigma_3 = \sigma_r \text{ with } \sigma_r = 0 \tag{4.4}$$

$$\sigma_a > \sigma_r \tag{4.5}$$

σ_1, σ_2 and σ_3 are the principal stresses of the stress state; respectively major, intermediate and minor stress.

The radial stress was applied using a fluid pressure system where confinement is provided using hydraulic oil. The axial load was applied through the loading piston with a 1 MN MTS servo-hydraulic load frame (MTS System Corporation). The experiment was monitored using a closed-looped and data acquisition system.

During the test, the following measurements were recorded:

- Internal load applied to the specimen (Input: Internal load cell)
- Vertical and lateral displacement of the specimen (Input: LVDTs)
- Axial and transversal strain of the specimen (Input: Strain gages)
- Fluid pressure applied to the specimen (i.e. σ_3) (Input: Hydraulic intensifier)
- Displacement of the linear bearing (Input: LVDT)

It is noted that the test was stroke controlled using a displacement rate of 0.0005 $\mathrm{m\,s^{-1}}$, which was monitored from the average of the two vertical LVDTs measurements.

4.5 Tests results

For the purpose of this study, four experiments in the Plane-Strain Apparatus were performed: one true-triaxial test ran under plane strain condition, one “un-conventional” triaxial test and two attempts of true-triaxial test under constant mean-stress.

4.5.1 True-triaxial experiment under plane strain condition

The true-triaxial experiment under plane strain condition was performed at with a minor stress (i.e. σ_3) magnitude of 10 MPa. Table 4.1 summarize the results of the experiments by presenting the stress state at achieved at failure of the specimen.

Test	σ_1 [MPa]	σ_2 [MPa]	σ_3 [MPa]	p [MPa]	q [MPa]	$\theta°$
TT1	88.14	46.85	10	48.33	55.28	28.12

Table 4.1: Results of the true-triaxial experiment under plane-strain condition

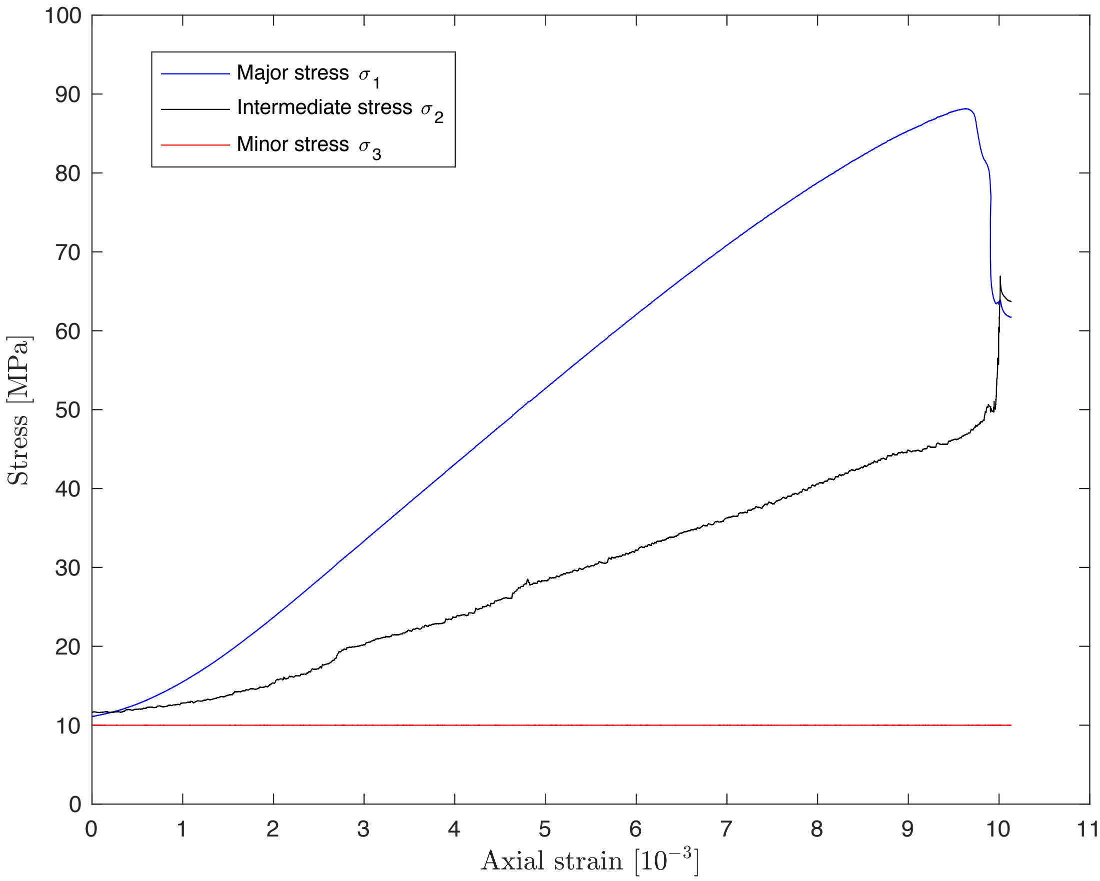

Figure 4.10: $\sigma - \epsilon_a$ plot for the true-triaxial experiment performed under plane strain condition

The stress-strain plot, presented in Figure 4.10, shows the evolution of the three principal stresses after the hydrostatic loading at 10 MPa. After reaching its peak value, the axial stress decreased rapidly which reveals the brittle post-peak behavior of the rock subject to this state of stress. By keeping $\epsilon_2 = 0$ through the test (cf. Figure 4.11), the intermediate stress increased linearly until the major stress reached its peak value. At this point, failure of the specimen is achieved and the strain ϵ_2 increase so does the intermediate stress. The minor stress was kept constant in accordance with the experiment conditions requirements.

Figure 4.12 shows the failed specimen from the side exposed to pistons that applied the intermediate stress, i.e. from the (σ_3-σ_2) plane where the failure surface formed. The specimen presents a kink in the failure surface at the middle of the specimen, leading to two different angles of failure (75° and 65°). This "non-unique" failure angle can be explained by two different orientation of the cracks that initiated failure at the top and bottom edges of the

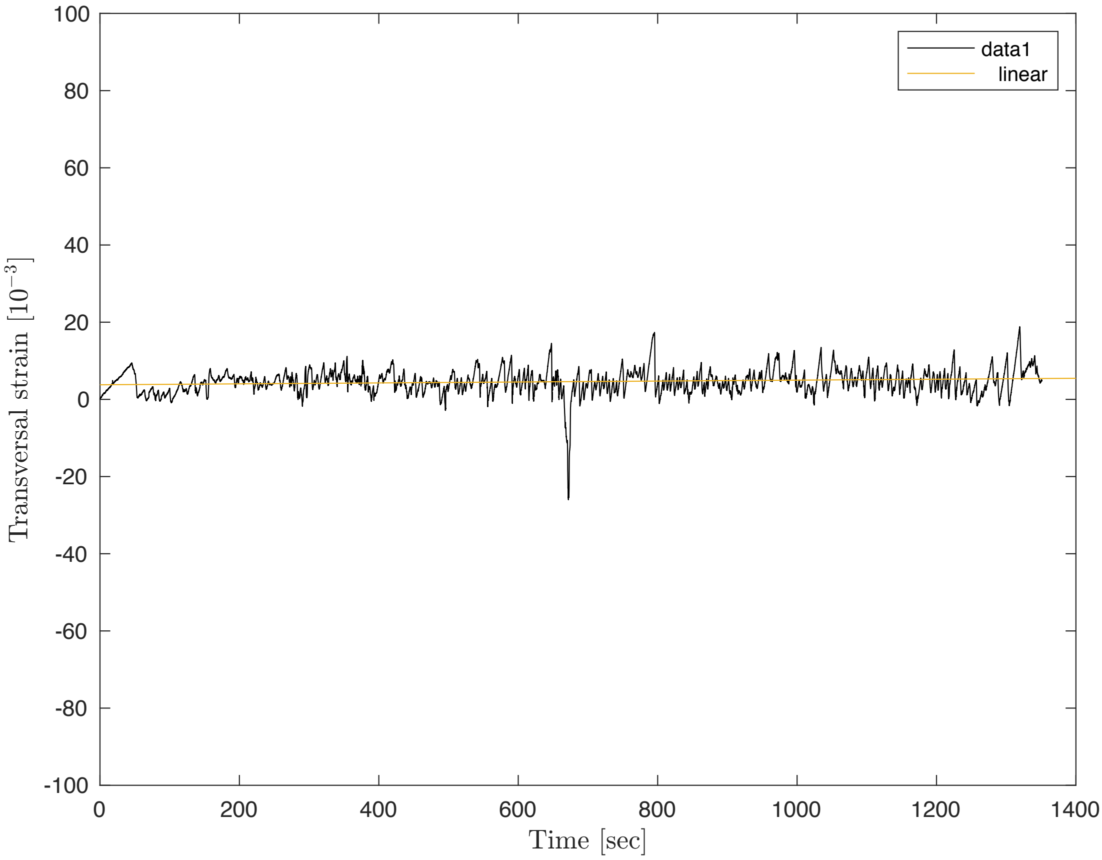

Figure 4.11: ϵ - time plot for true-triaxial experiment under plane strain condition

Test	σ_1 [MPa]	σ_2 [MPa]	σ_3 [MPa]	p [MPa]	q [MPa]	$\theta°$
TT 2	99.95	20	20	46.65	62.28	0

Table 4.2: Results of the “un-conventional” triaxial experiment

specimen and gathered at its center.

4.5.2 “Un-conventional” triaxial experiment

The “un-conventional” triaxial test was performed at a confining stress (i.e. $\sigma_2 = \sigma_3$) of 20 MPa. This minor stress was chosen to be close to the highest value allowed by the pressure cell capacity, which was 24 MPa. Table 4.2 summarize the results of the experiments by presenting the stress state at achieved at failure of the specimen.

The stress-strain plot, presented in Figure 4.13, shows the evolution of the three principal stresses after the hydrostatic loading at 20 MPa. After the axial stress reached a peak value of 99.95 MPa, it started to decrease before stabilizing around 95 MPa This post-peak tendency of the axial stress can be explained by the dilatancy of the specimen along the failure surface

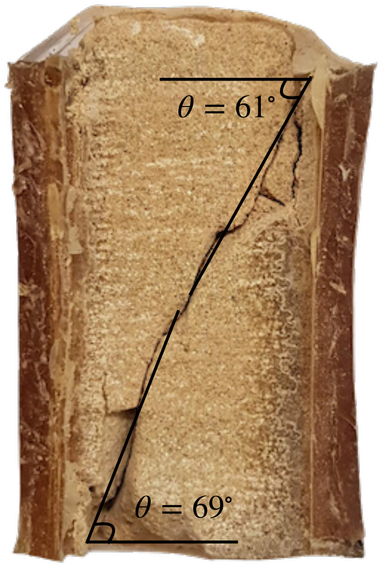

Figure 4.12: Failure surface of the TT 1 specimen

after it was formed, and the use of stroke control during the experiment. Indeed, as the specimen failure is initiated, its pieces along the failure surface slide apart and were pushed by the confining stress against the platens. However, the loading piston still moves at constant rate, which led to an increase in axial stress. The minor and intermediate stresses were kept constant in accordance with the experiment conditions requirements.

Figure 4.14 shows the failed specimen a) from the side perpendicular to the minor stress direction, and b) from the bottom (perpendicular to the axial stress). It presents a failure surface oriented at 66°, starting from the top right and ending at the bottom middle of the specimen.

For this experiment, two lateral LVDTs were added to the apparatus instrumentation. With their measurement of strain in the minor stress (i.e. σ_3) direction, the volumetric strain and the bulk modulus of the specimen were computed. The Bulk modulus is defined as follow:

$$K = \frac{p}{\epsilon_V} \tag{4.6}$$

where p is the mean stress (cf. Equation (2.8) 2.20) and the volumetric strain. Figure 4.15 presents the (p-ϵ_v) plot from which the Bulk modulus was computed, giving $K = 6.9\,\mathrm{GPa}$.

A comparison with the conventional triaxial compression test performed at 20 MPa is presented in Table 4.3. It shows a difference of about 9 MPa in axial stress at peak, the highest being reached by the prismatic specimen in the Plane-Strain Apparatus.

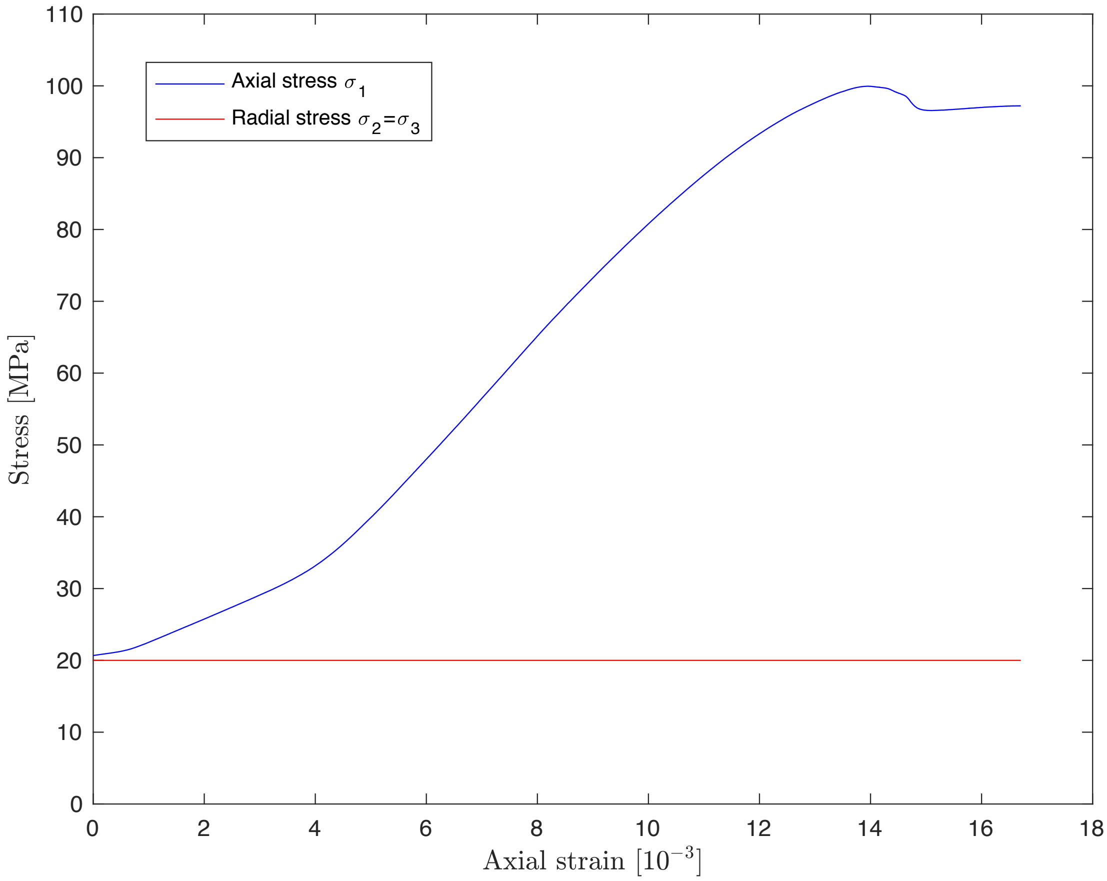

Figure 4.13: $\sigma - \epsilon_a$ plot for the “un-conventional” triaxial experiment

4.5.3 True-triaxial experiment under constant mean stress condition

Two not succeeding attempts to perform a true-triaxial test under constant mean stress condition were made for this study. This test results were supposed to be compared with the ones of the true-triaxial test performed under plane strain condition. Therefore, the stress path followed for this test was based on the state of stress reach at failure in the first one.

figure 4.16 schematically represents the procedure defined in section 4.4 The initial phase is a hydrostatic loading to achieve 10 MPa, which correspond to the minor stress applied in the first experiment. Starting from the second phase to the end, the minor stress is kept at 10 MPa. At the end of the second phase (i.e. “deviatoric” loading phase 2), the mean stress that would be kept constant until the end of the test, is achieved. For this test, the magnitude of the major

Test	σ_1 [MPa]	σ_2 [MPa]	σ_3 [MPa]	p [MPa]	q [MPa]	$\theta°$
TT 2	99.95	20	20	46.65	62.28	0
CTC 5	91.08	20	20	44.72	71.08	0

Table 4.3: Results of the true-triaxial experiment under plane-strain condition

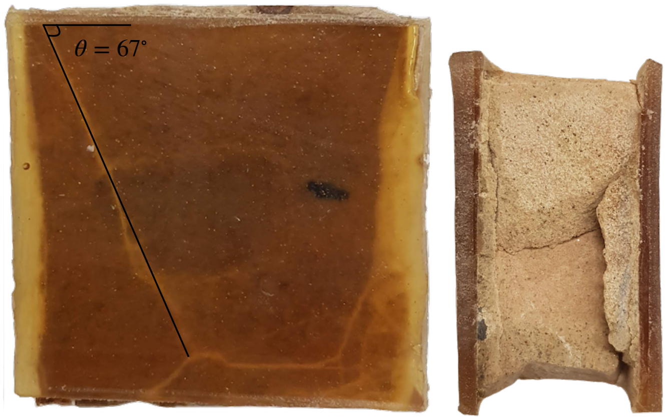

Figure 4.14: Failure surface of the TT2 specimen

and intermediate stresses at the end of this phase were back calculated from the mean stress at failure of the first test, following Equation

$$p_{TT1} = 44.5\,\text{MPa} \tag{4.7}$$

$$\sigma_3 = 10\,\text{MPa} \tag{4.8}$$

$$\sigma_{1,\text{init}} = \sigma_{2,\text{init}} = \sigma_{1,2} \tag{4.9}$$

$$p_{\text{initial}} = \frac{2\sigma_{1,2} - \sigma_3}{2} = 44.5\,\text{MPa} \tag{4.10}$$

$$\sigma_{1,2_{\text{int}}} = \frac{3p_{\text{initial}} - \sigma_3}{2} = 62\,\text{MPa} \tag{4.11}$$

The two attempts to perform this test were stopped during this second phase. Indeed, as the major and intermediate stresses were increased at the same rate to $\sigma_{1,2} = 62\,\text{MPa}$, σ_2 dropped the first time before reaching 55 MPa and the second time before 25 MPa. As suspected, they were a leak in the hydraulic pistons circuit. In the first attempt, one of them was out of its housing with the O-ring exposed and broken, and in the second, the other piston was out of its housing with the O-ring intact but exposed.

Three possible explanations can be brought to understand what happened. The first one questions the strength and capacity of the pistons. Indeed, although the indicated maximum capacity is 69 MPa, the first attempt showed that the leak happened before reaching this value. However, the second one leaked at low stress, and was small compared to the theoretical capacity of the pistons. The second explanation may be that the specimen failed before reaching this initialization step, which lead to think that the state of stress applied wasn't appropriate to the rock. However, no external sign of failure has been seen on the specimen. *It still might be a failure surface that we cannot see.* Finally, the third explanation may be that the specimen was not large enough, which forced the pistons to come out of their housing trying

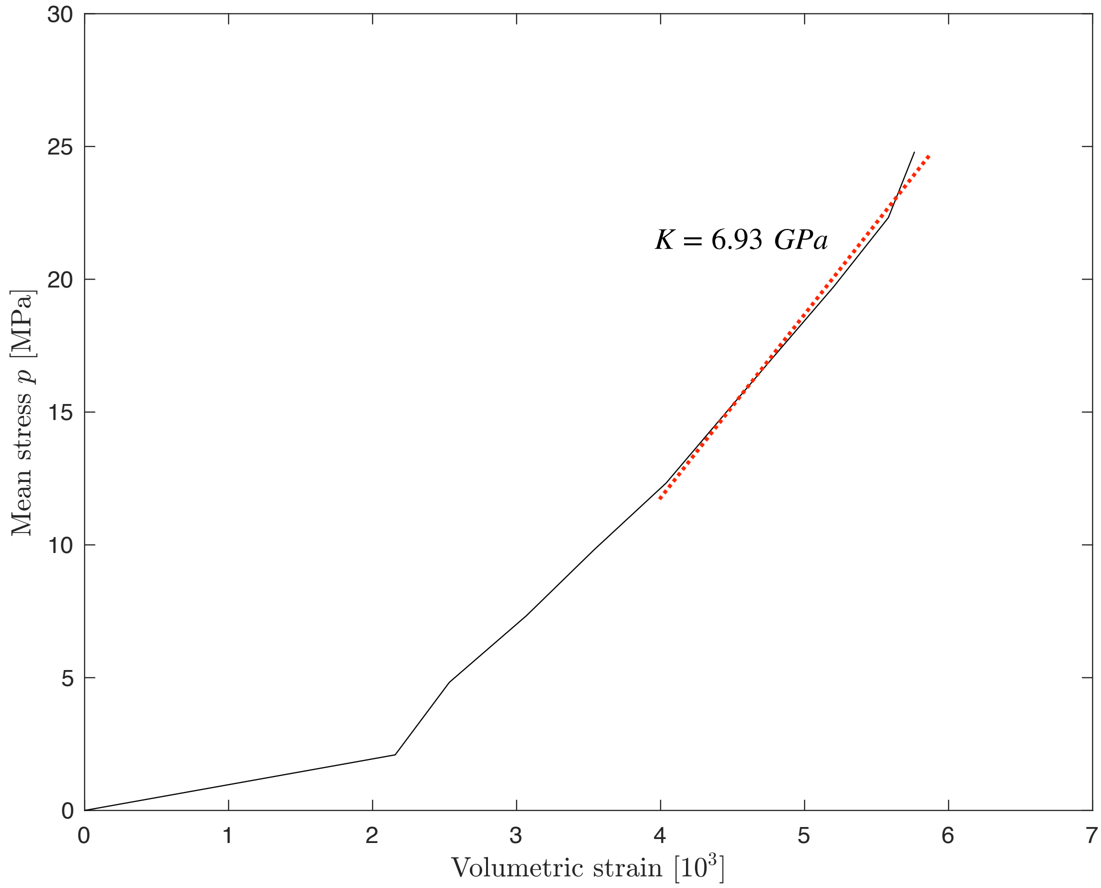

Figure 4.15: $p - \epsilon_V$ plot and computation of the Bulk modulus

to apply a higher stress.

Although this experiment wasn't successful, previous ones performed in the Plane Strain Apparatus were. Some adjustments of the apparatus, the specimen or the procedure should be made to enable performing true-triaxial tests under constant mean stress condition.

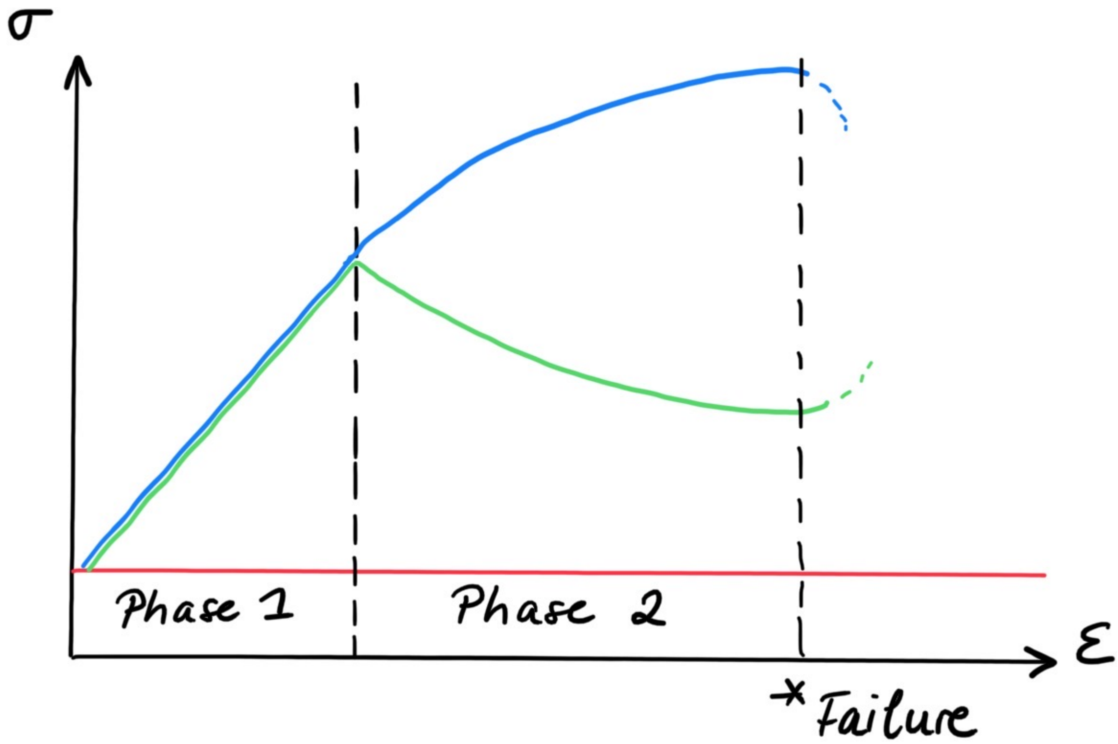

Figure 4.16: Sketch of the procedure for true-triaxial experiment under constant mean stress condition

5 Results and Discussion

5.1 Experiments results Database

The main objective of this study was to propose an evaluation of three failure criteria for a selected rock, Dunnville Sandstone. As explained in the previous chapters, their empirical nature requires a thick database of diverse multi axial experiments for their development.

Dunnville Sandstone have been used for several works in the past and particularly for multi axial experiments [1][3][2]. The ones performed in the scope of this study (cf. Chapter 4) presented the opportunity to enrich the existing tests results database and to evaluate the failure criteria with data representative of Dunnville Sandstone response.

The database presented in Table 5.1 was based on the one proposed by Zeng et al. (2019) [3], and extended with the results of the experiments from this study. In this table, each experiment is associated with the following elements: the orientation of the bedding regarding the application of the axial stress, the three principal stresses (i.e. σ_I,σ_{II},σ_{III}) and the stress invariants (i.e.p, q, θ).

This database was used for the evaluation of Mohr-Coulomb,Hoek-Brown and Paul-Mohr-Coulomb failure criteria, that will be presented in the following sections.

5.2 Evaluation of the failure criteria

The Mohr-Coulomb, Hoek-Brown and Paul-Mohr-Coulomb failure criteria presented in Chapter 2 were fitted to the experiment results of Dunnville Sandstone from Table 5.1. A computation program was developed for the fittings using the programming language Python. All the resources needed to access the program files are listed in Appendix REFAPPENDIX B.

The three failure criterion fittings are evaluated through their representation in the three coordinates systems presented in Chapter 2, and their accuracy in terms of how good they fit the data. In this study, this "accuracy" is chosen to be evaluated by comparing the least mean

Test	Bedding	σ_I [MPa]	σ_{II} [MPa]	σ_{III} [MPa]	p [MPa]	q [MPa]	θ [°]
Published TC-1	⊥	29.7	0.0	0.0	9.9	29.7	0
Published TC-2	⊥	39.4	2.5	2.5	14.8	36.9	0
Published TC-3	⊥	52.9	5.0	5.0	21.0	47.9	0
Published TC-4	⊥	71.5	10.0	10.0	30.5	61.5	0
Published TC-5	⊥	98.4	20.0	20.0	46.1	78.4	0
Published TC-6	⊥	114.5	30.0	30.0	58.2	84.5	0
Published TC-7	⊥	129.4	40.0	40.0	69.8	89.4	0
Published TC-8	⊥	142.1	50.0	50.0	80.7	92.1	0
Published TC-9	⊥	153.8	60.0	60.0	91.3	93.8	0
Published TC-10	∥	24.9	0.0	0.0	8.3	24.9	0
Published TC-11	∥	35.2	2.5	2.5	13.4	32.7	0
Published TC-12	∥	48.8	5.0	5.0	19.6	43.8	0
Published TC-13	∥	68.0	10.0	10.0	29.3	58.0	0
Published TC-14	∥	95.9	20.0	20.0	45.3	75.9	0
Published TC-15	∥	110.9	30.0	30.0	57.0	80.9	0
Published TC-16	∥	125.5	40.0	40.0	68.5	85.5	0
Published TC-17	∥	138.1	50.0	50.0	79.4	88.1	0
Published TC-18	∥	150.8	60.0	60.0	90.3	90.8	0
UCS	⊥	29.8	0	0	27.95	51.43	0
TC 9	⊥	49.43	5	5	19.81	44.43	0
TC 0	⊥	61.43	10	10	27.95	51.43	0
TC 5	⊥	91.08	20	20	44.72	71.08	0
TC 8	⊥	127.3	40	40	65.73	87.30	0
TC 10	⊥	151.1	60	60	88.12	91.10	0
Published TE-1	⊥	35.0	35.0	0.8	23.6	34.2	60
Published TE-2	⊥	40.0	40.0	1.2	27.1	38.8	60
Published TE-3	⊥	50.0	50.0	6.0	35.3	44.0	60
Published TE-4	⊥	60.0	60.0	10.1	43.4	49.9	60
Published TE-5	⊥	69.0	69.0	11.5	49.8	57.5	60
Published TE-6	∥	40.0	40.0	1.8	27.3	38.2	60
Published TE-7	∥	50.0	50.0	5.7	35.2	44.3	60
Published TE-8	∥	60.0	60.0	8.0	42.7	52.0	60
TE 3	⊥	35	35	3.96	24.64	31.08	60
TE 1	⊥	40	40	4.50	27.89	36.34	60
TE 2	⊥	60	60	9.68	43.01	50.98	60
Published TT-1	⊥	48.3	31.6	5.0	28.3	37.8	37.5
Published TT-2	⊥	52.9	25.1	7.0	28.3	40.1	22.7
Published TT-3	⊥	63.9	12.1	9.0	28.3	53.4	2.9
Published TT-4	⊥	70.6	49.4	15.0	45.0	48.7	37.8
Published TT-5	⊥	77.5	70.5	20.0	56.0	54.3	53.5
Published TT-6	⊥	83.9	62.1	22.0	56.0	54.4	39.7
TT 1	⊥	88.14	46.85	10	48.33	55.28	28.12
TT 2	⊥	99.98	20	20	46.65	62.28	0

Table 5.1: Database of experiments results for Dunnville Sandstone. The "Published" data are from Zeng et al. [3]

standard deviation misfits, as proposed by Benz et al. (2008) [15].

The standard deviation s_i of one test series i formed by j experiments subject to the same minor stress (i.e. σ_{III}) is defined by Equation 5.1. In this expression, n is the number of experiments in the test series i, $\sigma_{I,j}^{\text{test}}$ is the maximum stress at failure for a data point j (obtained from the database) and $\sigma_{I,j}^{\text{calc}}$ is the calculated one using the considered criterion formulation.

$$s_i = \sqrt{\frac{1}{n}\sum_j \left(\sigma_{I,j}^{\text{calc}} - \sigma_{I,j}^{\text{test}}\right)^2} \tag{5.1}$$

Finally, the mean standard deviation misfit is computed following Equation 5.2, where m is the number of test series. The smallest the $\bar{S}$ is , the better is the prediction of the model for the rock compared to other criteria. A criterion that would perfectly fit the data will present no misfits.

$$\bar{S} = \frac{1}{m}\sum_i s_i \tag{5.2}$$

5.2.1 Mohr-Coulomb failure criterion

The Mohr-Coulomb failure criterion is formulated in terms two principal stresses (cf. Equations 2.17 and 2.18) and unique strength parameters (i.e. ϕ,c), therefore, the fitting was done using only axisymmetric triaxial compression tests results (i.e. $\theta = 0°$).

From this fitting, the coefficient K_p was determined and the other parameters were computed:

$$K_p = 2.55 \quad \text{and} \quad C_0 = 29.7\,\text{MPa} \tag{5.3}$$

$$\phi = \frac{K_p - 1}{K_p + 1} = 25.9° \tag{5.4}$$

$$c = \frac{C_0(1 - sin\phi)}{2cos\phi} = 9.30\,\text{MPa} \tag{5.5}$$

$$V_0 = \frac{C_0}{K_p - 1} = 19.2\,\text{MPa} \tag{5.6}$$

Knowing the strength parameters, the Mohr-Coulomb failure surface is plotted in the $(\sigma_3 - \sigma_1)$ plane using Equation 2.17(cf. Figure 5.1).

The criterion was also fitted in the $(p - q)$ plane, for which the plot obtained is shown in Figure

5.2. The coefficients $m_{c,e}$ and $b_{c,e}$ were computed using Equations 2.27 to 2.30:

$$m_c = \frac{6\sin\phi}{3-\sin\phi} = 1.02 \tag{5.7}$$

$$m_e = \frac{6\sin\phi}{3+\sin\phi} = 0.76 \tag{5.8}$$

$$b_c = \frac{6c\cos\phi}{3-\sin\phi} = 19.6\,\text{MPa} \tag{5.9}$$

$$b_e = \frac{6c\cos\phi}{3+\sin\phi} = 14.6\,\text{MPa} \tag{5.10}$$

Finally, the Mohr-Coulomb criterion is presented in the π-plane, obtained following the procedure described in Section 2.2.3. Figure 5.3 shows Mohr-Coulomb failure criterion in the pi-plane at different values of the mean stress p.

The mean standard deviation misfit obtained with the Mohr-Coulomb failure criterion is 14.0 [MPa].

5.2.2 Hoek-Brown failure criterion

The Hoek-Brown failure criterion is also formulated in terms two principal stresses (cf. Equations 2.31) and unique strength parameters (i.e. m, C_0), therefore, the fitting was done using only axisymmetric triaxial compression tests results (i.e. $\theta = 0°$).

From this fitting, the strength parameter m was determined and V_0 was computed:

$$m = 5.96 \quad \text{and} \quad C_0 = 29.7\,\text{MPa} \tag{5.11}$$

$$V_0 = \frac{C_0}{m} = 4.98\,\text{MPa} \tag{5.12}$$

Knowing the strength parameters, the Hoek-Brown failure surface is plotted in the $(\sigma_3 - \sigma_1)$ plane using Equations 2.32 for the compression line and 2.33 for extension (cf. Figure 5.1).

In the $(p-q)$ plane, the Hoek-Brown failure criterion is plotted using Equations 2.36 for compression and 2.37 for extension, and showed in Figure 5.5. These surfaces are expressed in terms of m and C_0 previously defined.

Finally, the Hoek-Brown criterion is presented in the π-plane, obtained following the procedure described in Section 2.3.3. Figure 5.6 shows Hoek-Brown failure criterion in the pi-plane at different values of the mean stress p.

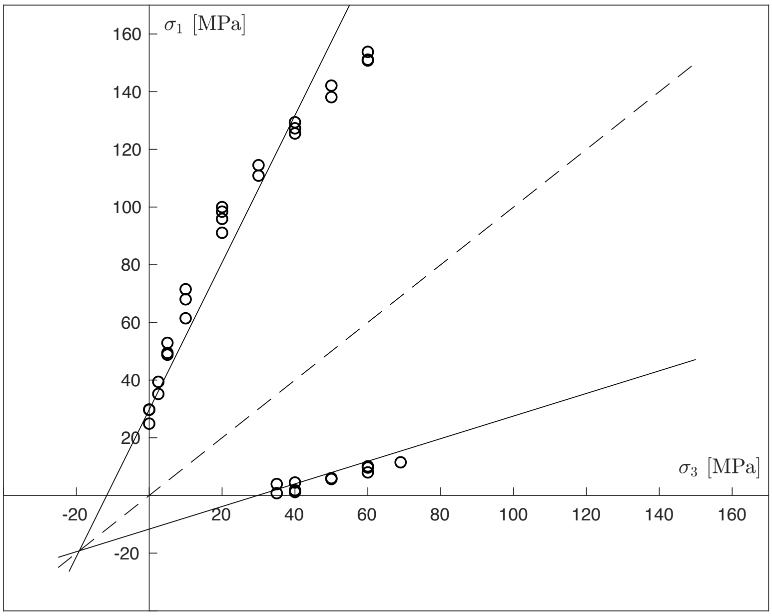

Figure 5.1: Mohr-Coulomb criterion failure surface in $(\sigma_3 - \sigma_1)$ plane

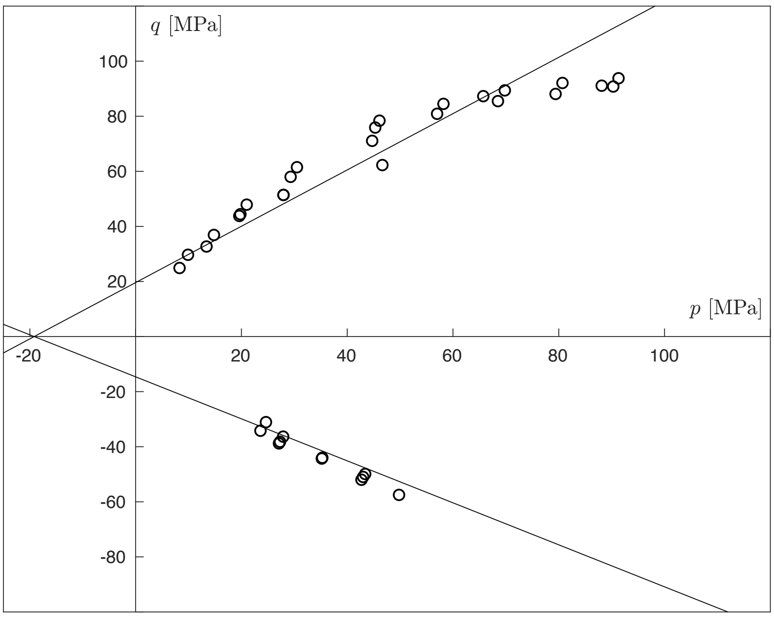

Figure 5.2: Mohr-Coulomb criterion failure surface in $(p - q)$ plane

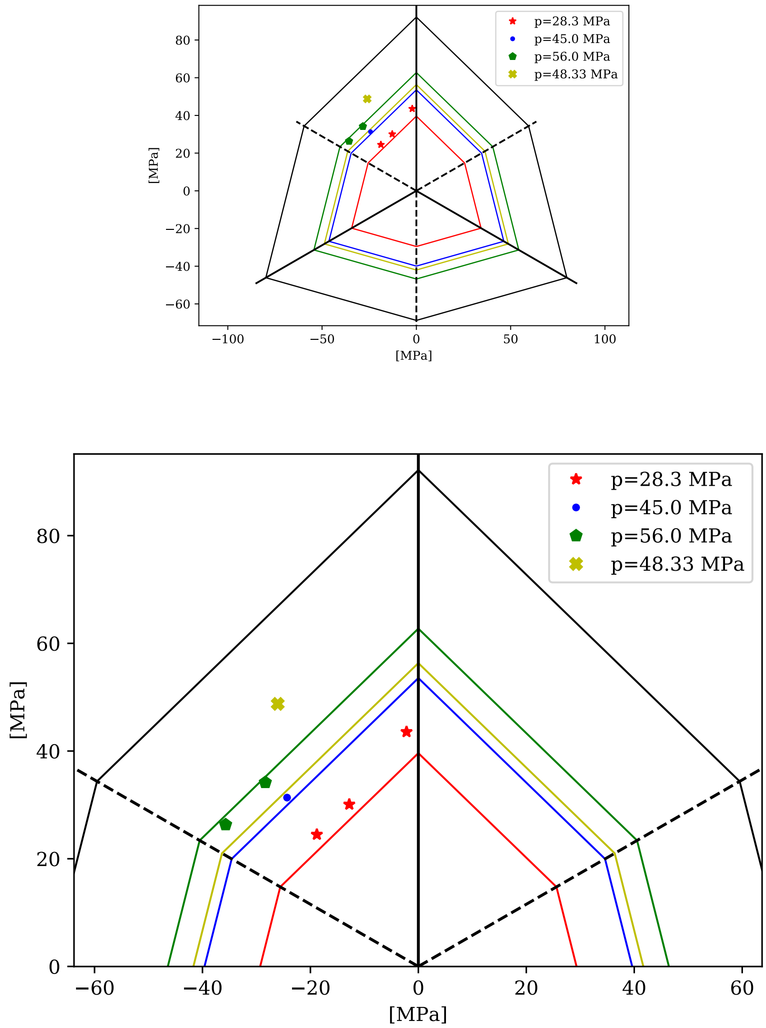

Figure 5.3: Mohr-Coulomb criterion failure surface in π-plane

The mean standard deviation misfit obtained with the Hoek-Brown failure criterion is 9.37 [MPa].

5.2.3 Paul-Mohr-Coulomb failure criterion

Contrary to the previous criteria, the Paul-Mohr-Coulomb failure criterion is formulated in terms the three principal stresses (cf. Equations 2.38 and 2.43) and non-unique strength parameters (i.e. $\phi_{c,e}$, $c_{c,e}$, V_0), therefore, the fitting was done using all tests results from the database.

From the least-square solution fitting describe in Chapter 2 (cf. Section 2.4.3, Equations 2.52

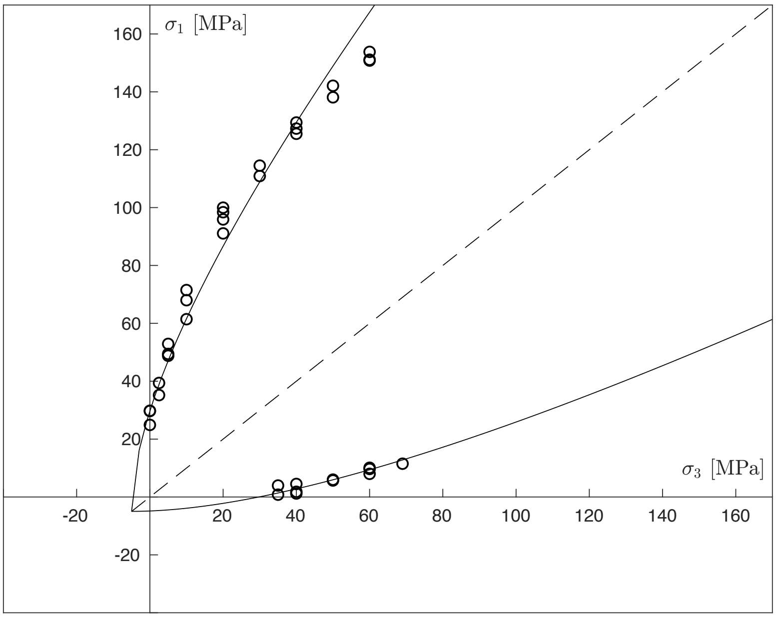

Figure 5.4: Hoek-Brown criterion failure surface in $(\sigma_3 - \sigma_1)$ plane

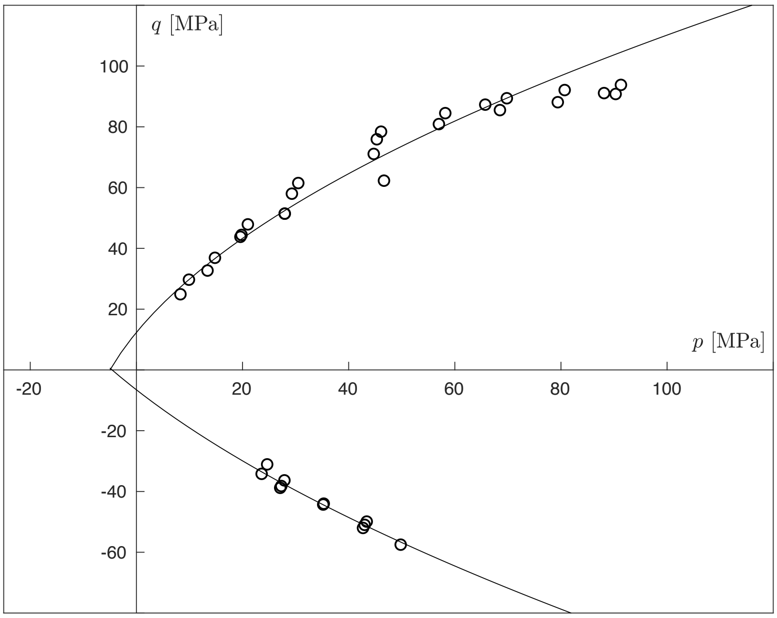

Figure 5.5: Hoek-Brown criterion failure surface in $(p - q)$ plane

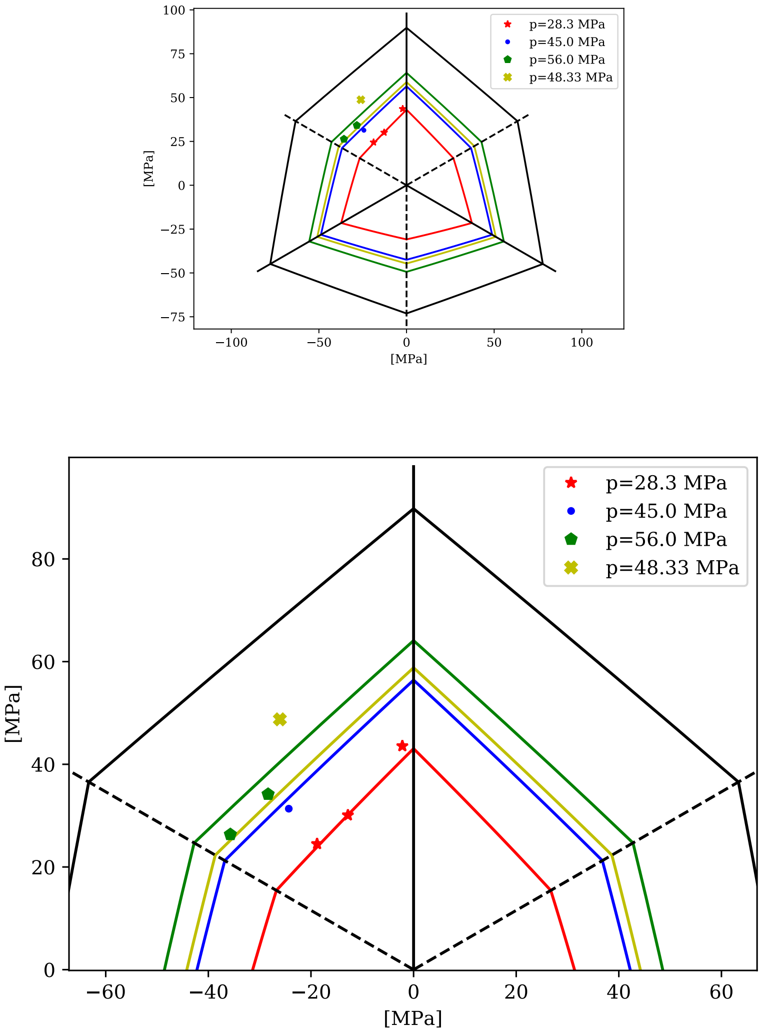

Figure 5.6: Hoek-Brown criterion failure surface in π-plane

and 2.57), the following solution could be obtained:

$$x_1 = \frac{b_c}{V_0} = 0.81 \tag{5.13}$$

$$x_2 = k = -0.91 \tag{5.14}$$

$$x_3 = b_c = 28.77\,\text{MPa} \tag{5.15}$$

Following Equations 2.56 to 2.60, the strength parameters for Paul-Mohr-Coulomb failure criteria could be computed:

$$V_0 = \frac{0.81}{b_c} = 35.62\,\mathrm{MPa} \tag{5.16}$$

$$b_e = \frac{2b_c}{(1-\sqrt{3}k)} = 22.31\,\mathrm{MPa} \tag{5.17}$$

$$\phi_c = arcsin\left(\frac{3b_c}{6V_0 + b_c}\right) = 20.85° \tag{5.18}$$

$$\phi_e = arcsin\left(\frac{3b_e}{6V_0 - b_c}\right) = 20.85° \tag{5.19}$$

$$c_c = \frac{b_c\left(3 - \sin\phi_c\right)}{6\cos\phi_c} = 13.57\,\mathrm{MPa} \tag{5.20}$$

$$c_e = \frac{b_e\left(3 + \sin\phi_e\right)}{6\cos\phi_e} = 10.52\,\mathrm{MPa} \tag{5.21}$$

Knowing the strength parameters, the Paul-Mohr-Coulomb failure surface could be plotted in the $(\sigma_3 - \sigma_1)$ plane using Equations 2.44 to 2.46. The graph obtained, using the coefficients computed in Equations 5.22 to 5.25, is presented in Figure 5.7.

$$M_c = \frac{1 + \sin\phi_c}{1 - \sin\phi_c} = 2.11 \tag{5.22}$$

$$M_e = \frac{1 + \sin\phi_e}{1 - \sin\phi_e} = 2.08 \tag{5.23}$$

$$C_c = \frac{2c_c \cos\phi_c}{1 - \sin\phi_c} = 39.38\,\mathrm{MPa} \tag{5.24}$$

$$C_e = \frac{2c_e \cos\phi_e}{1 - \sin\phi_e} = 30.31\,\mathrm{MPa} \tag{5.25}$$

In the $(p - q)$ plane, the Paul-Mohr-Coulomb failure criterion is plotted using Equations 2.49 to 2.51, and the graph obtained in presented in Figure 5.8. These surfaces are expressed in terms of $b_{c,e}$,defined by Equations 5.15 and 5.17, and $m_{c,e}$ computes as follow:

$$m_c = \frac{6\sin\phi_c}{3 - \sin\phi_c} = 0.81 \tag{5.26}$$

$$m_e = \frac{6\sin\phi_e}{3 - \sin\phi_e} = 0.63 \tag{5.27}$$

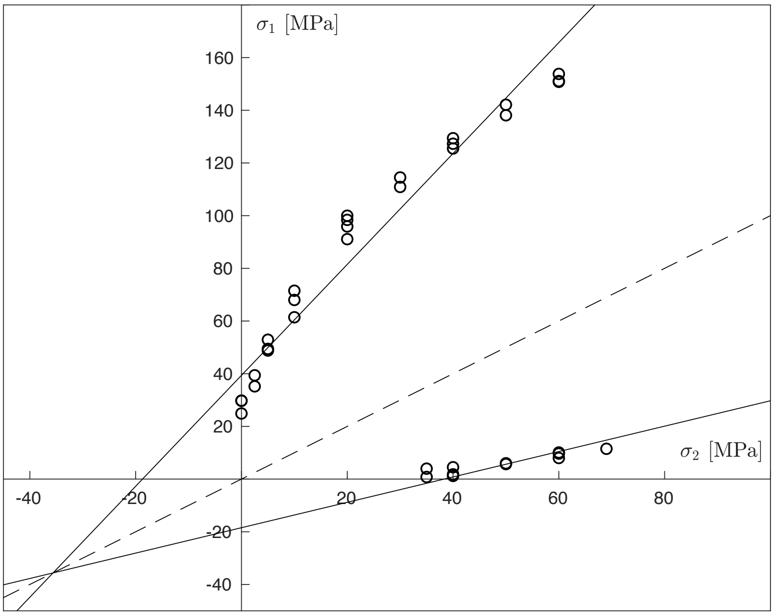

Figure 5.7: Paul-Mohr-Coulomb criterion failure surface in $(\sigma_3 - \sigma_1)$ plane

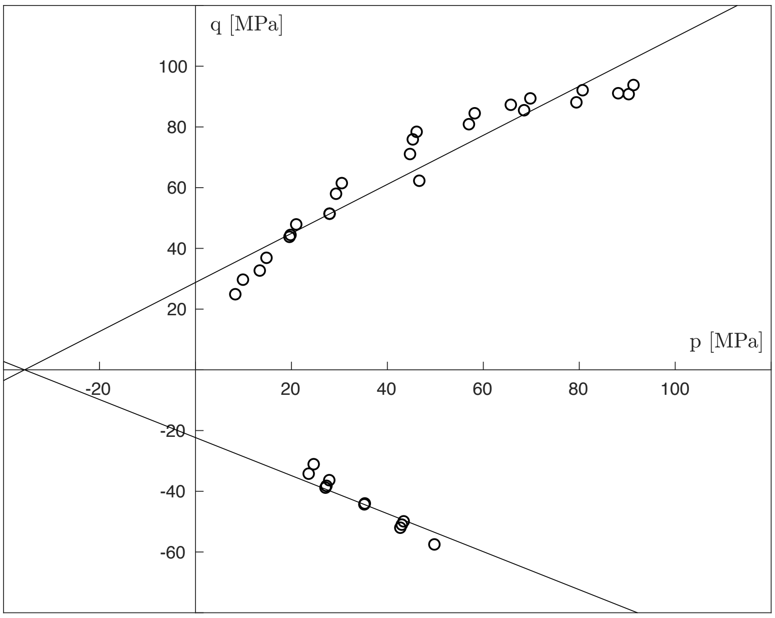

Figure 5.8: Paul-Mohr-Coulomb criterion failure surface in $(p - q)$ plane

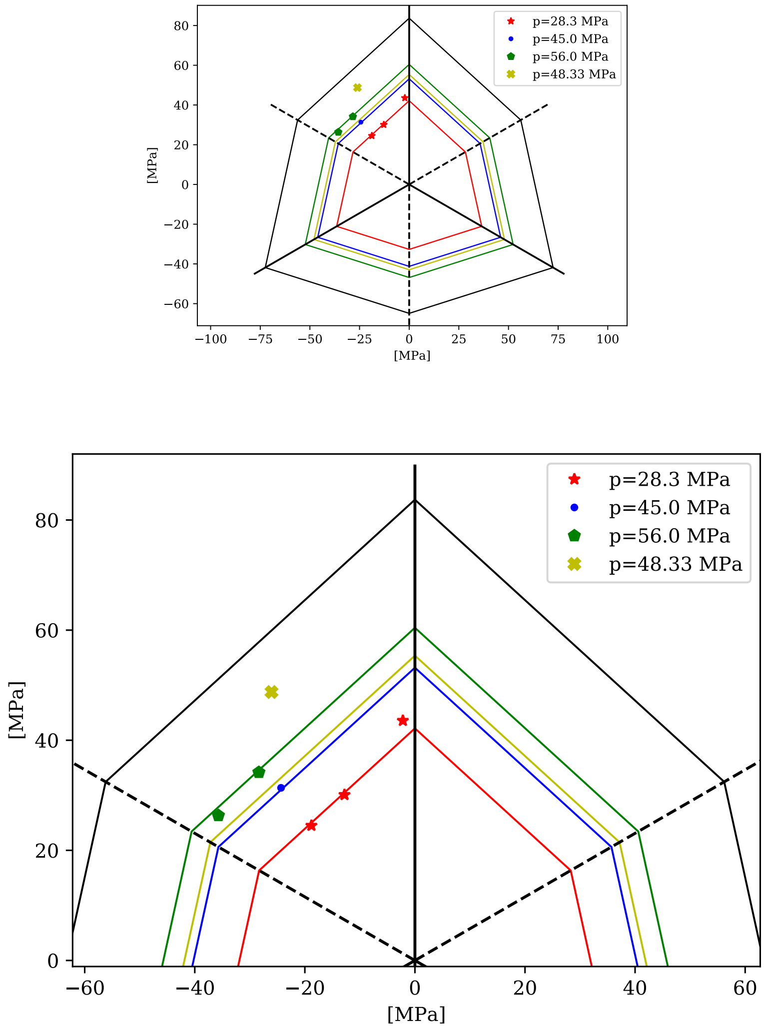

Figure 5.9: Paul-Mohr-Coulomb criterion failure surface in π-plane

Finally, the Paul-Mohr-Coulomb criterion is presented in the π-plane, obtained following the procedure described in Section 2.4. Figure 5.9 shows the failure criterion in the π-plane at different mean stresses p, corresponding to true-triaxial experiments mean stresses at failure (i.e. data points where $0° < \theta < 60°$ in Table 5.1).

The mean standard deviation misfit obtained with the Paul-Mohr-Coulomb failure criterion is 13.2 [MPa].

5.2.4 Comparison of the failure criteria

The mean standard deviation misfits obtained for the three failure criteria show that Hoek-Brown provide a better approximation of the data points (cf. Table 5.2). However, it should

Criterion	Mean standard deviation misfit $\bar{S}$
Mohr-Coulomb	14.0
Hoek-Brown	9.37
Paul-Mohr-Coulomb	13.2

Table 5.2: Summary of the mean standard deviation misfits obtained for the three failure criteria evaluated

be kept in mind that this criterion was fitted only for data points related to axisymmetric compression experiments. Therefore, its prediction of true triaxial experiments is less accurate than the one provided by the Paul-Mohr-Coulomb criterion. This can be easily noticed with the observation of both predictions in the π-plane (cf. Figures 5.6 and 5.9).

5.3 Bi-linear Paul-Mohr-Coulomb failure criterion

Published data from multi axial experiments on multiple rocks showed that the failure envelop that describe them best is not linear over a large range of mean stress. However, popular failure theories as Mohr-Coulomb or Hoek-Brown, are either linear or do not provide an accurate prediction for all mean stresses. In this study, Paul-Mohr-Coulomb failure criteria is chosen to respond to this issue by approximating the nonlinear failure surface in a piecewise linear manner, resulting in a failure surface defined by six parameters.

5.3.1 Paul-Mohr-Coulomb with six parameters

The theoretical background on the six parameters Paul-Mohr-Coulom criterion presented in this section is based on the work of Labuz et al. (2018) [1].

The Paul-Mohr-Coulomb failure criterion presented in the Section 5.2.3 is referred to as Paul-Mohr-Coulomb with three parameters, which failure surface is a plane defined by the general equation of the criterion (cf. Equation 2.43), using three strength parameters : V_0, ϕ_c and ϕ_e. The Paul-Mohr-Coulomb failure surface defined in a piecewise manner is, therefore, made of a minimum of two plane each expressed using three strength parameters, leading to the six parameters criterion.

The three parameters criterion definition in terms of the three principal stresses describes a regular 6-sided pyramid in the principal stresses three-dimensional space (cf. Section 2.1). Therefore, by adding a plane to the failure surface, the six parameters criterion describes two irregular 6-sided pyramids. Each plane is then defined by the parameters presented in Table 5.3, where $P2$ indicates the plane that approximate data points at low mean stress and $P1$ the ones at higher mean stress. Table 5.4 present four types of Paul-Mohr-Coulomb failure surfaces which can be defined according to the values of the parameters. For all types, the

Plane	$P1$	$P2$
Friction angle in compression	$\phi_c^{(1)}$	$\phi_c^{(2)}$
Friction angle in extension	$\phi_e^{(1)}$	$\phi_e^{(2)}$
Theoretical uniaxial tensile strength	$V_0^{(1)}$	$V_0^{(2)}$

Table 5.3: Parameters of the planes defining the failure surface of Paul-Mohr-Coulomb criterion

Type of failure surface	Parameters conditions
(i) 6-sided	$V_0^{(1)} = V_0^{(2)}$
(ii) 6-12-6 sided	$\phi_c^{(1)} < \phi_c^{(2)}, \phi_e^{(1)} < \phi_e^{(2)}, p_c \neq p_e$
(iii) 6-12 sided	$(\phi_c^{(1)} < \phi_c^{(2)}, \phi_e^{(1)} \geq \phi_e^{(2)})$ or $(\phi_c^{(1)} \geq \phi_c^{(2)}, \phi_e^{(1)} < \phi_e^{(2)})$
(iv) 6-12-6 sided	$\phi_c^{(1)} < \phi_c^{(2)}, \phi_e^{(1)} < \phi_e^{(2)}, p_c = p_e$

Table 5.4: Types of failure surfaces for the six parameters Paul-Mohr-Coulomb criterion

following conditions apply:

$$V_0^{(1)} > V_0^{(2)} \quad \text{and} \quad 0° \leq \phi_{c,e}^{(i)} \leq 60° \tag{5.28}$$

The complete graphical representation of the Paul-Mohr-Coulomb failure surface is composed of the $(p-q)$ plane, the $(\sigma_2-\sigma_1)$ plane, the π-plane and the principal stresses three-dimensional space. The transition between $P2$ and $P1$ is well represented in the $(p-q)$ plane, where they intersect on the compression side (i.e. $q > 0$) at the mean stress value p_c and on the extension side (i.e. $q < 0$) at p_e. In the case of the failure surface type (ii), these transitions points have different values leading to a 12 sided transition zone on the pyramid for mean stress values $p \in [p_c; p_e]$. Sketches of the 6-12-6 sided failure surface in different planes and in the three-dimensional space are presented in Figure 5.10, where the $(\sqrt{3}p-\sigma^*)$ plane is equivalent to the $(p-q)$ plane. More schematic representations and details on the four failure surfaces types are provided in APPENDIX C REFAPPENDIX C.

The addition of the intermediate stress in the Paul-Mohr-Coulomb general equation (cf. Equation 2.38) makes relevant the representation of the criterion in the $(\sigma_2-\sigma_1)$ plane. Indeed, this plane presents the advantage to gather the data points for axisymmetric experiments, shown on compression and extension lines, as well as true-triaxial data in the same plot (cf. Figure 5.11). The Paul-Mohr-Coulomb failure surfaces are plotted for a chosen value of σ_3,

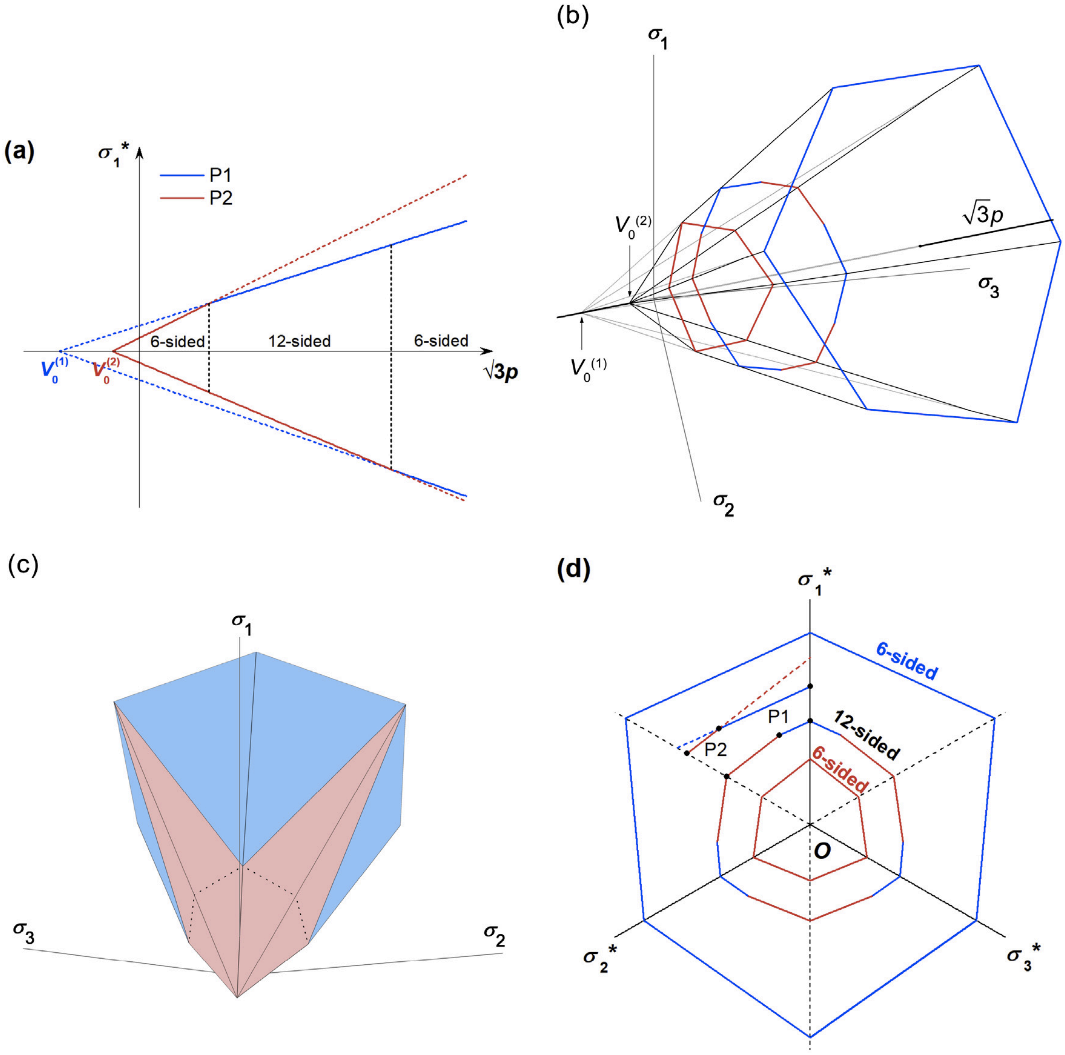

Figure 5.10: Paul-Mohr-Coulomb 6-12-6 sided failure surface graphical representations

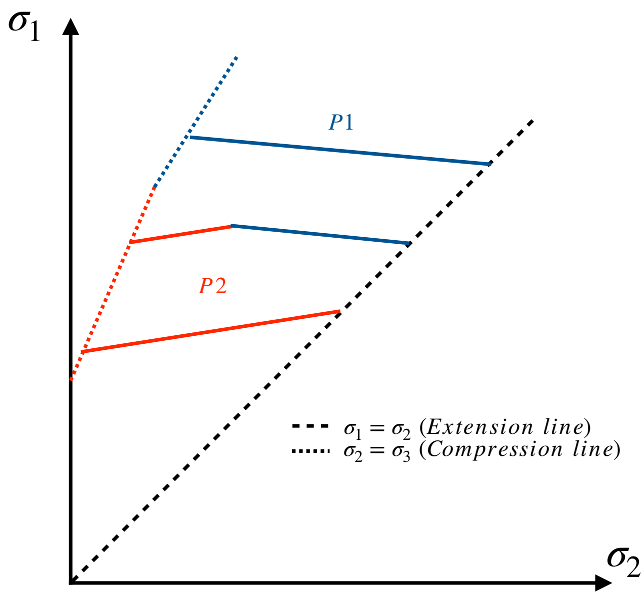

Figure 5.11: Paul-Mohr-Coulomb 6-12-6 sided failure surface in $(\sigma_2 - \sigma_1)$ plane

using the following equation, based the rearrangement of Equation 2.38:

$$\sigma_1 = \frac{1}{A}(1 - B\sigma_2 - C\sigma_3) \tag{5.29}$$

5.3.2 Bi-linear fitting program

The fitting of a six-parameters Paul-Mohr-Coulomb failure surface requires to create two datasets from the initial database of experiments results, one for each plane. Once defined, these datasets are used for planes fitting, following the procedure presented in Section 2.4.3. This repartition of the data points into different planes is a challenging step of the failure criterion fitting, as it should give the optimal solution for the database considered.

One of this study objective was to create a program that automatically allocates data points to one of both planes, with the aim of getting a distribution that provide the best fitting for Paul-Mohr-Coulomb criterion. Moreover, it was crucial that this program was develop not only for the rock tested for this study (i.e. Dunnville Sandstone), but for any rock with available experimental data.

This problem can be summarize by the following question:

How to automatize the allocation of data point into $P1$ or $P2$ in order to provide the most accurate fitting of Paul-Mohr-Coulomb criterion ?

In the following paragraphs, the algorithm created to solve this problem will be described.

Algorithm construction

The algorithm developed to solve the problem presented above belongs to the *Brute-force* algorithm family. This category is based on the following principal: every possibility offered by the database is tried and the one that gives the best solution to the problem is selected. The amount of data available in the case of rock testing ($n_{max} \sim 50$) is small enough to use this type of algorithm without having issues related to too high complexity.

In the case of this study, the algorithm will test all the possible variations of data allocations to the $P1$ or $P2$ datasets which can be created form the rock database. For each possible combination, planes $P1$ and $P2$ are created by the computation of their coefficient and fitting parameters defined for Paul-Mohr-Coulomb, following the procedure presented in 2.4.3. Then, the Mean Square Error (MSE) is computed for each combination of datasets. Finally the data allocation variation that provides the minimal MSE is selected as the solution of the two planes fitting problem.

The algorithm proposed in this study can be apply to any rock testing database that contains results of the three principal stresses and the three invariants at failure (cf. Table 5.1). Indeed, the rock database is the only input that is required to run this algorithm.

Computation of the mean square error

The error used in the computation of MSE is equal to the distance of a data point, defined by σ_I, σ_{II} and σ_{III}, from its belonging plane, defined by Equation 2.38:

$$err_i = A^{(j)}\sigma_I^i + B^{(j)}\sigma_{II}^i + C^{(j)}\sigma_{III}^i - 1 \tag{5.30}$$

where i is the index of the data point in the database and j indicates the plane number in which the data is allocated (i.e. $j = 1$ for $P1$ and $j = 2$ for $P2$). The Mean Square Error of a certain dataset combination k is then computed as follow:

$$MSE_k = \frac{1}{n}\sum_{i=1}^{n} err_i^2 \tag{5.31}$$

The dataset combination k that obtains the minimal MSE value provides the best fitting solution for Paul-Mohr-Coulomb failure surface for the considered rock.

Program resources

This algorithm was implemented in the programming language Python. The resources on the program developed to solve the two planes fitting problem are gathered in APPENDIX B. It contains the Python files required to run the program and a *README* document that explains how to use the program. Moreover, all the code files are commented in detail to ease their use and understanding.

5.3.3 Dunnville Sandstone

The program presented in the previous section was applied to the experimental results database of Dunnville Sandstone (cf. Table 5.1). The six parameters Paul-Mohr-Coulomb failure surface obtained is presented in the following paragraphs through its representation in the $(p-q)$, $(\sigma_2-\sigma_1)$, π- planes and in the principal stresses three-dimensional space.

Strength parameters computation

The solution obtained from the least-square solution fitting describe in Chapter 2 (cf. Section 2.4.3, Equations 2.52 and 2.57) is presented in Table 5.5.

The strength parameters for Paul-Mohr-Coulomb failure criteria could be computed from Equations 2.56 to 2.60. The values obtained are gathered in Table 5.6.

Graphical representation of the failure surface

Knowing the strength parameters, the Paul-Mohr-Coulomb failure surface could be plotted in the $(p-q)$ plane using Equations 2.49 to 2.51 applied to each plane. The values of parameters $m_{c,e}$ and $c_{c,e}$ are presented in Table 5.7 and the $(p-q)$ plane plot is shown in Figure 5.12.

The failure surface can also be plotted in the $(\sigma_2-\sigma_1)$ plane. Equation 5.29 provides the planes equation in this coordinates system using the general expression of the Paul-Mohr-Coulomb criterion, which coefficients A, B and C are presented in Table 5.8. Figure 5.13 presents the six parameters failure surface for Dunnville Sandstone in the $(\sigma_2-\sigma_1)$ plane.

The failure surface planes are also presented in the π-plane, obtained following the procedure described in Section 2.4. Figure 5.14 shows the failure criterion in the π-plane at different mean stresses p that correspond to true-triaxial experiments mean stresses at failure (i.e. $0° < \theta < 60°$ in Table 5.1). In addition, Figure 5.15 presents the projection of the $P2$,$P2-P1$ transition and $P1$ pyramids on the π-plane.

Finally, Figure 5.16 shows the 6-12-6 sided pyramid obtained for Dunnville Sandstone in the three-dimensional space.

A summary of the Paul-Mohr-Coulomb six parameters solution and the mean standard deviation misfits obtained for Dunnville Sandstone is presented in Table 5.9. The fittings provided by Mohr-Coulomb, Hoek-Brown, three and six parameters Paul-Mohr-Coulomb criteria can now be compared using the mean standard deviation misfits values obtained (cf. Table 5.2). The

Plane	$x_1^{(i)}$	$x_2^{(i)}$	$x_3^{(i)}$
$P1$	0.54	-1.02	47.08
$P2$	1.39	-1.10	15.47

Table 5.5: $P1$ and $P2$ least-square solutions x for Dunnville sandstone

Plane	$b_c^{(i)}$ [MPa]	$b_e^{(i)}$ [MPa]	$V_0^{(i)}$ [MPa]	$\phi_c^{(i)}$ [°]	$\phi_e^{(i)}$ [°]
$P1$	47.1	34.1	86.9	14.4	12.1
$P2$	15.5	10.7	11.1	34.3	34.8

Table 5.6: $P1$ and $P2$ strength parameters for Dunnville sandstone

Plane	$m_c^{(i)}$ [-]	$m_e^{(i)}$ [-]	$c_c^{(i)}$ [MPa]	$c_e^{(i)}$ [MPa]
$P1$	0.54	0.39	22.3	16.2
$P2$	1.39	0.96	7.61	5.26

Table 5.7: $P1$ and $P2$ fitting parameters for Dunnville sandstone

Plane	$A^{(i)}$	$B^{(i)}$	$B^{(i)}$
$P1$	1.74×10^{-2}	4.26×10^{-3}	-3.32×10^{-2}
$P2$	3.47×10^{-2}	-8.31×10^{-4}	-1.24×10^{-1}

Table 5.8: Paul-Mohr-Coulomb general equation coefficients for Dunnville sandstone

Plane	$V_0^{(i)}$ [MPa]	$\phi_c^{(i)}$ [°]	$\phi_e^{(i)}$ [°]	$\bar{S}$ [MPa]
$P1$	86.9	14.4	12.1	9.12
$P2$	11.1	34.3	34.8	4.92

Table 5.9: $P1$ and $P2$ strength parameters for Dunnville sandstone

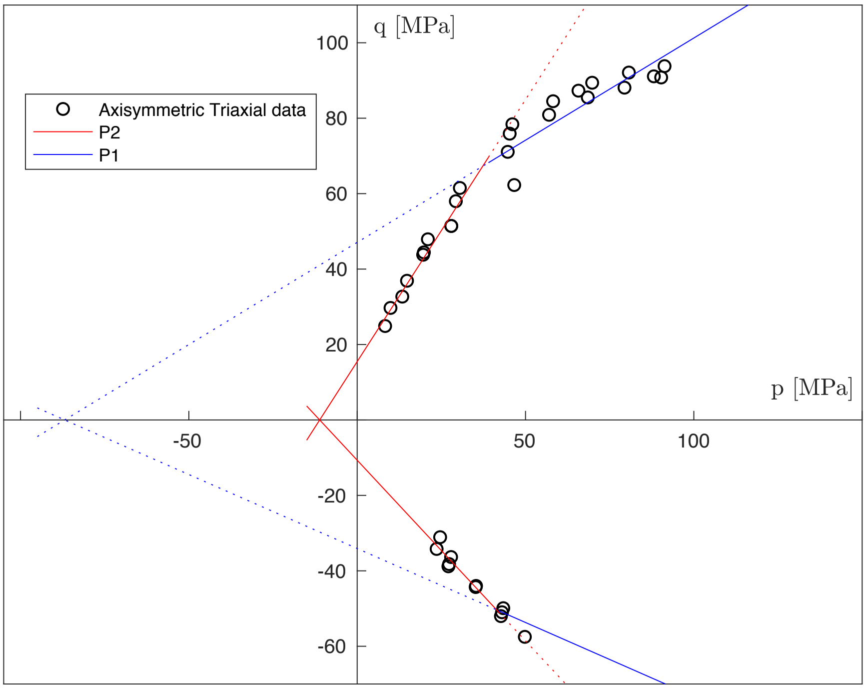

Figure 5.12: Paul-Mohr-Coulomb failure surface in the $(p-q)$ plane for Dunnville Sandstone

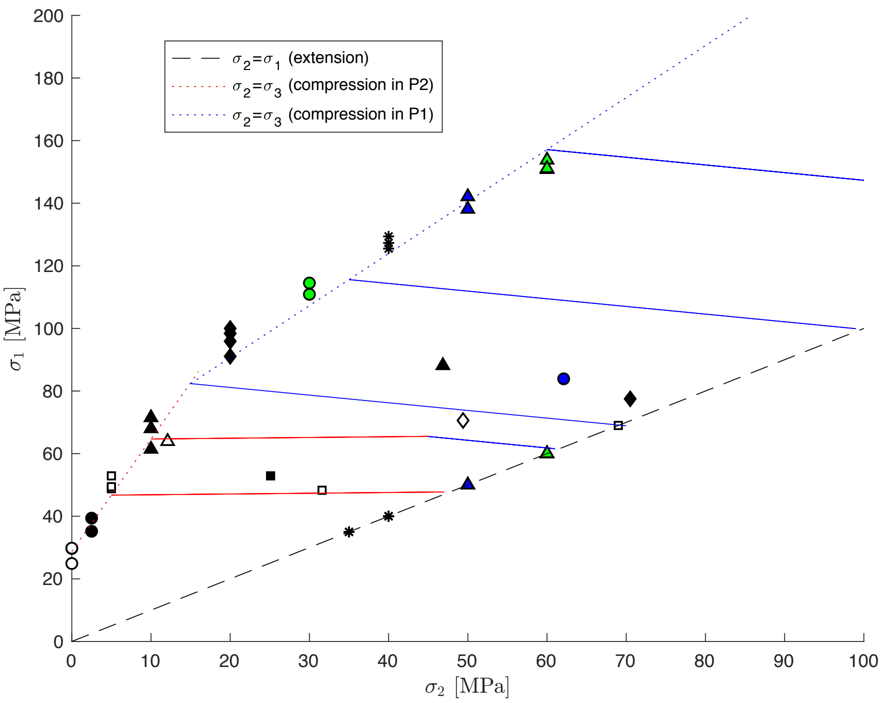

Figure 5.13: Paul-Mohr-Coulomb failure surface in the $(\sigma_2-\sigma_1)$ plane for Dunnville Sandstone

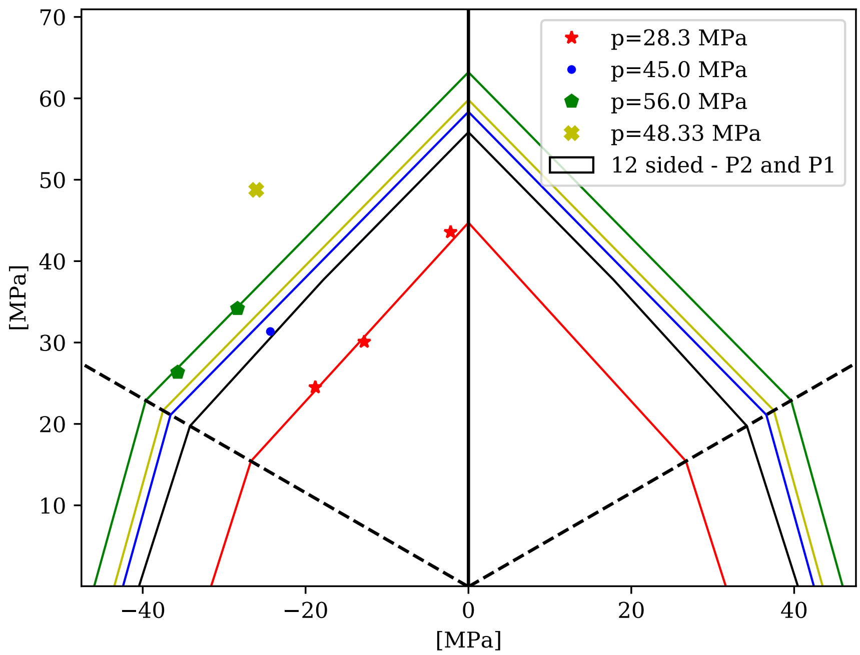

Figure 5.14: Paul-Mohr-Coulomb failure surface in the π-plane for Dunnville Sandstone

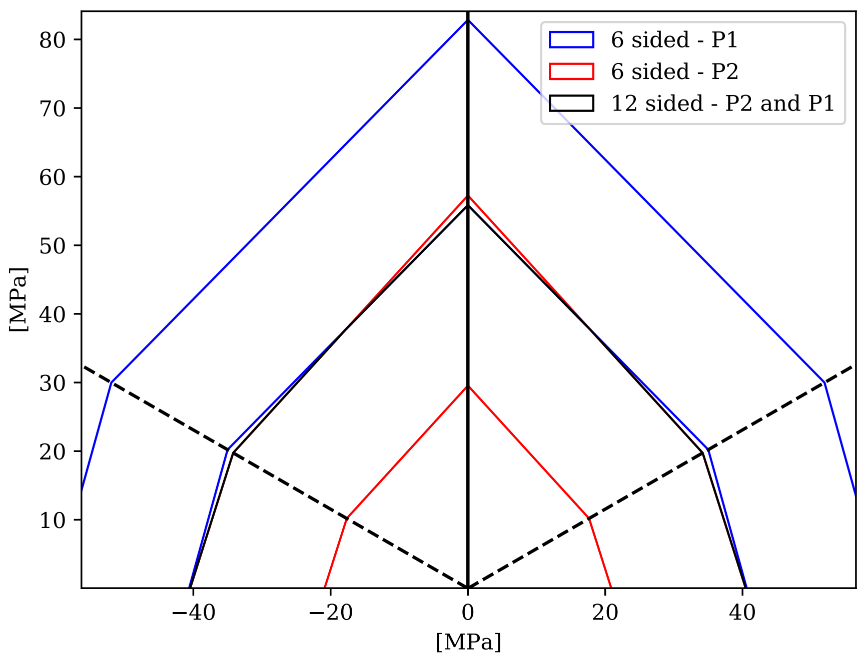

Figure 5.15: 6-12-6 sided pyramid projection in the π-plane for Dunnville Sandstone

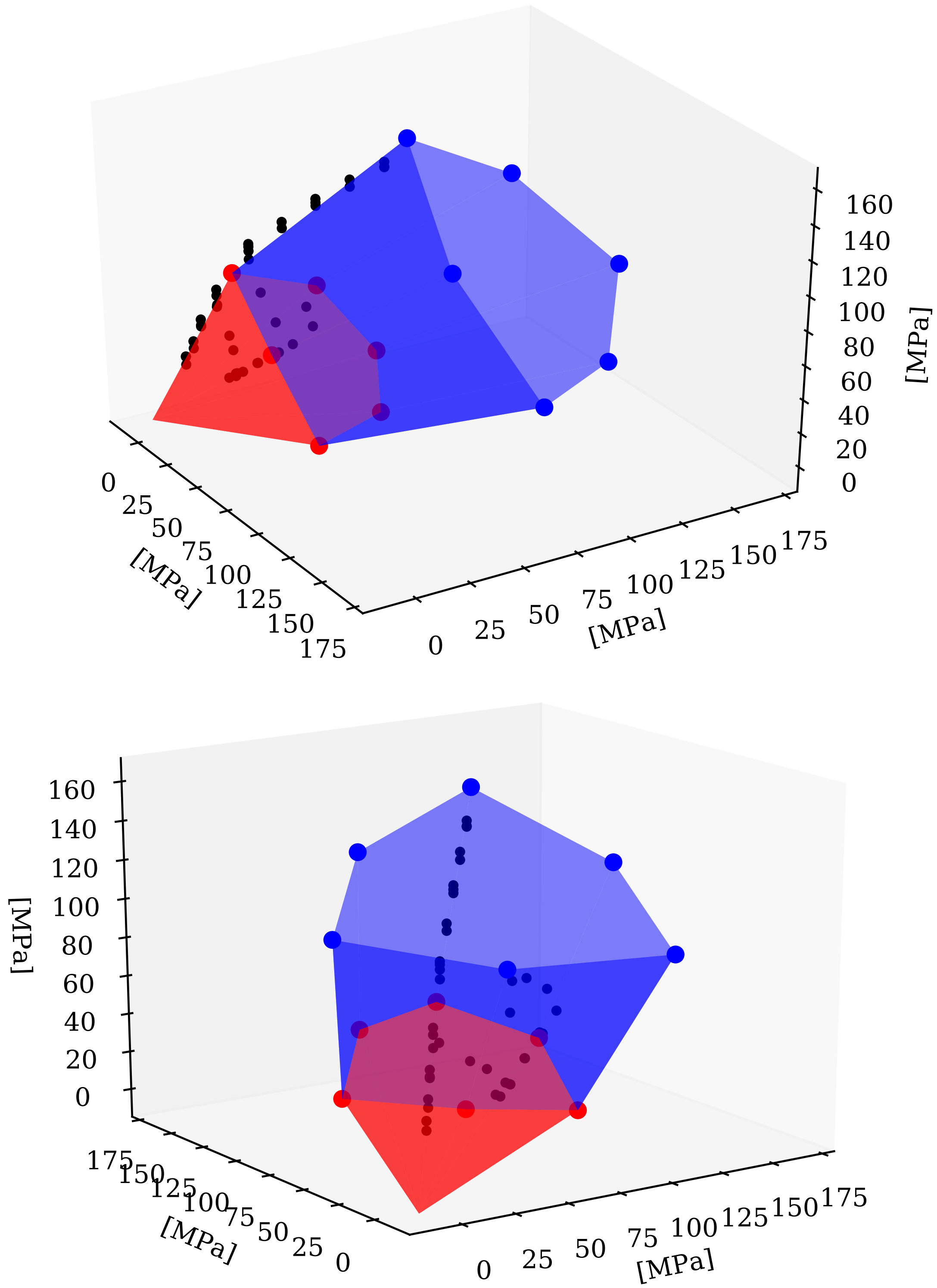

Figure 5.16: Paul-Mohr-Coulomb 6-12-6 sided failure surface pyramid for Dunnville Sandstone

six parameters Paul-Mohr-Coulomb criterion provides the best prediction with the least mean standard deviation misfits for the two planes. This can be explained by the combination of the intermediate stress inclusion in the failure criterion general equation and the approximation of the failure surface non linearity, giving the most accurate states of stress prediction at failure. The observation of the six parameters Paul-Mohr-Coulomb and Hoek-Brown fittings in the $(p-q)$ and π- planes also presents for the first one a better approximation of the true-triaxial data points, but also of the axisymmetric ones, which wasn't the case with the three parameters Paul-Mohr-Coulomb.

The program developed for the Paul-Mohr-Coulomb criterion was generalized so it can be used to fit of other rocks. A summary of the results obtained for rocks with available database from literature is provided in APPENDIX D REFAPPENDIX D.

5.4 Discussion

In this section, some remarks and comments are made on the work presented in this study.

The previous sections provide a comparison of the four failure criteria principally based on the computation of the mean standard deviation misfits $\bar{S}$. This quantitive comparison indicator is based on the computation of the error between the predicted and real values of the major stress, and report the precision of the prediction provided by a failure criterion. Another comparison could also be relative to the failure surface. Indeed, a more rigorous evaluation of a failure criterion can be made by the computation of the distance between a data point and the failure surface. This type of error computation was used in this work in the *Brute-force* algorithm developed for the six parameters Paul-Mohr-Coulomb fitting (cf. Section 5.3.2). In this case, as well as for Mohr-Coulomb, the computation of the "point-plane" distance is made possible and convenient thanks to the explicit general equation of the planes that forms the failure surface. However, in the case of Hoek-Brown and other criteria defined by implicit equations, it becomes challenging to go through the mathematical derivations required. An interesting addition to this work would be to look at all the criteria evaluated here from the point of view of the "data-failure surface" distance, and to compare the quantitative indicators of the their accuracy.

The comparison of the three failure criteria revealed the importance of taking into account the intermediate stress in their formulation. First, the evaluation of the Mohr-Coulomb and Paul-Mohr-Coulomb indicates that even with the use of a linear criterion to approximate a non-linear failure surface, the one defined by a general equation in terms of the three principal stresses gives a better approximation of the data points. Moreover, the comparison between the Hoek-Brown and Paul-Mohr-Coulomb fittings reveals that a linear criterion that takes into account σ_{II} gives a better fitting of the data from true triaxial experiments, which state of stress is more representative of what undergoes the rock in-situ.

The work presented in this study showed that the six parameters Paul-Mohr-Coulomb failure criterion provides an accurate approximation of the failure surface as well as a good prediction of the state of stress at failure compared to popular criteria as Mohr-Coulomb and Hoek-Brown. Nonetheless, one criticism can be addressed to this criterion regarding the amount of experiments required to construct the bi-linear failure surface. Indeed, in order to built the failure surface of the three parameters Paul-Mohr-Coulomb criterion, three data points are needed, leading to a requirement of six points for the six parameters criterion. These six data points corresponds to the same number of experiments, ideally of different procedures, that is needed to be performed on the same rock. By carrying out this study in an very well equipped research environment, it was possible to perform multiple experiments under different conditions. However, this is hardly the case in the majority of rock mechanics and geo-engineering applications for which that amount of data is not always available. From this point of view, Mohr-Coulomb and Hoek-brown are more convenient to apply to a small amount of data, which is why they are popular and widely use.

On the π-plane representations of the failure criteria (cf. Figure 5.14) the data point of the true triaxial experiment under plane strain condition (i.e. $p = 48.3$ MPa) presents an eccentricity from the failure surface but also from the "alignment" or "group" of other true-triaxial data (mainly performed under constant mean stress). Two possible explanation are proposed here. One can be that a mistake was made either during the experiment or in the analysis of its results. The second notices the possibility that the failure surface underestimate data from this type of experiments. Both highlight the need of an more detailed investigation on true triaxial experiments performed under various state of stress. However, it should be noted that preforming true triaxial experiments is challenging and time consuming, which makes difficult to gather data for the same rock.

Finally, a general comment can be made on the use of failure criteria. The not successful attempts made at performing a true triaxial experiment under constant mean stress pointed out the importance of failure stress state prediction. Indeed, the state of stress at failure should have been checked before running the test, revealing foreseen values of σ_I and σ_{II} to be reached, too close to failure of the specimen. Prediction of rock failure is crucial in geo-engineering applications, and research work should continue to seek for the best general failure criteria.

6 Conclusion

Bibliography

[1] J. F. Labuz, F. Zeng, R. Makhnenko, and Y. Li, "Brittle failure of rock: A review and general linear criterion," *Journal of Structural Geology*, vol. 112, pp. 7–28, jul 2018. doi: 10.1016/j.jsg.2018.04.007

[2] A. Tarokh, "Poro-elastic response of saturated rock." phdthesis, Department of Civil, Environmental and Geo-Engineering, University of Minnesota, 2016, p.71.

[3] F. Zeng, B. L. Folta, and J. F. Labuz, "Strength testing of sandstone under multi-axial stress states," *Geotechnical and Geological Engineering*, vol. 37, no. 6, pp. 4803–4814, may 2019. doi: 10.1007/s10706-019-00939-5

[4] C. J. Jaeger and N. G. W. Cook, *Fundamentals of Rock Mechanics, 3rd edition.* Chapman and Hall, 1979.

[5] J. Labuz, S.-T. Dai, and E. Papamichos, "Plane-strain compression of rock-like materials," *International Journal of Rock Mechanics and Mining Sciences & Geomechanics Abstracts*, vol. 33, no. 6, pp. 573–584, sep 1996. doi: 10.1016/0148-9062(96)00012-5

[6] R. Makhnenko and J. Labuz, "Plane strain testing with passive restraint," *Rock Mechanics and Rock Engineering*, vol. 47, no. 6, pp. 2021–2029, nov 2013. doi: 10.1007/s00603-013-0508-2

[7] B. Paul, "Generalized pyramidal fracture and yield criteria," *International Journal of Solids and Structures*, vol. 4, pp. 175–196, 1968.

[8] J. P. Meyer and J. F. Labuz, "Linear failure criteria with three principal stresses," *International Journal of Rock Mechanics and Mining Sciences*, vol. 60, pp. 180–187, jun 2013. doi: 10.1016/j.ijrmms.2012.12.040

[9] E. Hoek, E. T. Brown, and E. Vol, "Empirical strength criterion for rock masses," *Journal of the Geotechnical Engineering Division, ASCE.*, vol. 106, pp. 1013–1015, 1980.

[10] B. Folta, "Strength testing under multi-axial stress states," Master's thesis, Department of Civil, Environmental and Geo-Engineering, University of Minnesota, 2016. [Online]. Available: http://hdl.handle.net/11299/182131

[11] M. Ostrom, "Cambrian stratigraphy in western wisconsin," 1966. [Online]. Available: https://wgnhs.wisc.edu/pubs/download_ic07/

[12] R. Ulusay, "The isrm suggested methods for rock characterization, testing and monitoring: 2007-2014," *ISRM*, 2015.

[13] "Practices for preparing rock core as cylindrical test specimens and verifying conformance to dimensional and shape tolerances," 2019. doi: 10.1520/d4543-19

[14] J. Franklin and E. Hoek, "Developments in triaxial testing technique," *Rock mechanics*, vol. 2 (4), p. 223–228.

[15] T. Benz and R. Schwab, "A quantitative comparison of six rock failure criteria," *International Journal of Rock Mechanics and Mining Sciences*, vol. 45, no. 7, pp. 1176–1186, oct 2008. doi: https://doi.org/10.1016/j.ijrmms.2008.01.007